AD-A163 331 A THREE DIMENSIONAL PLASMA SIMULATION CODE APPLIED TO PHASE VELOCITY PRED (U) UTAH UNIV SALT LAKE CITY DEPT OF ELECTRICAL ENGINEERING P E PRINCE OCT 85 1/1

UNCLASSIFIED UTEC-85-049 RADC-TR-85-198 F30602-82-C-0161 F/G 20/3 NL

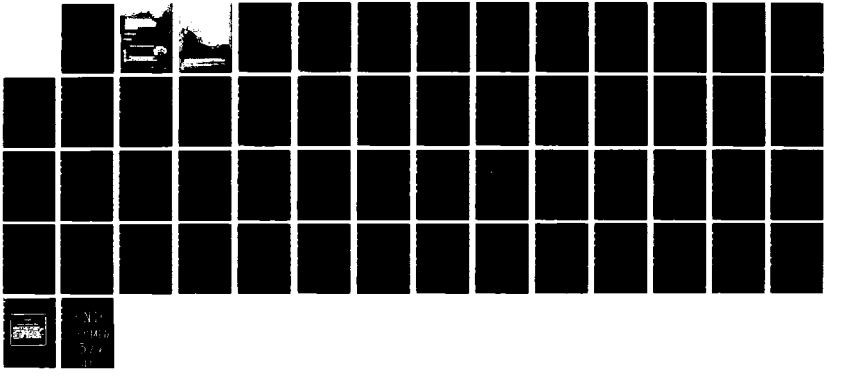

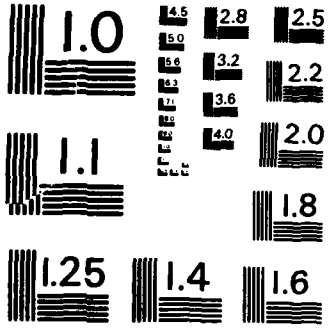

RADC-TR-85-198
Final Technical Report
October 1985

A THREE DIMENSIONAL PLASMA SIMULATION CODE APPLIED TO PHASE VELOCITY PREDICTION IN A COUPLED CAVITY CIRCUIT

University of Utah

Paul E. Prince

ROME AIR DEVELOPMENT CENTER
Air Force Systems Command
Griffiss Air Force Base, NY 13441-5700

UNCLASSIFIE
SECURITY CLASSIFICATION OF THIS PAGE

AD-A163 331

REPORT DOCUMENTATION PAGE

1a. REPORT SECURITY CLASSIFICATION UNCLASSIFIED	1b. RESTRICTIVE MARKINGS N/A
2a. SECURITY CLASSIFICATION AUTHORITY N/A	3 DISTRIBUTION / AVAILABILITY OF REPORT Approved for public release; distribution unlimited.
2b DECLASSIFICATION / DOWNGRADING SCHEDULE N/A	
4. PERFORMING ORGANIZATION REPORT NUMBER(S) UTEC 85-049	5. MONITORING ORGANIZATION REPORT NUMBER(S) RADC-TR-85-198
6a. NAME OF PERFORMING ORGANIZATION University of Utah Dept of Electrical Engineering 6b. OFFICE SYMBOL (If applicable)	7a. NAME OF MONITORING ORGANIZATION Rome Air Development Center (OCTP)
6c. ADDRESS (City, State, and ZIP Code) Salt Lake City UT 84112	7b ADDRESS (City, State, and ZIP Code) Griffiss AFB NY 13441-5700
8a. NAME OF FUNDING / SPONSORING ORGANIZATION AFOSR 8b. OFFICE SYMBOL (If applicable) NE	9 PROCUREMENT INSTRUMENT IDENTIFICATION NUMBER F30602-82-C-0161
8c. ADDRESS (City, State, and ZIP Code) Bolling AFB Wash DC 20332	10. SOURCE OF FUNDING NUMBERS PROGRAM ELEMENT NO: 61102F; PROJECT NO: 2305; TASK NO: J9; WORK UNIT ACCESSION NO: 16

11. TITLE (Include Security Classification)
A THREE DIMENSIONAL PLASMA SIMULATION CODE APPLIED TO PHASE VELOCITY PREDICTION IN A COUPLED CAVITY CIRCUIT

12. PERSONAL AUTHOR(S)
Paul E. Prince

13a. TYPE OF REPORT	13b. TIME COVERED	14. DATE OF REPORT (Year, Month, Day)	15. PAGE COUNT
Final	FROM Sep 82 TO Sep 85	October 1985	58

16. SUPPLEMENTARY NOTATION
Research accomplished in conjunction with Air Force Thermionics Engineering Research Program (AFTER)

17. COSATI CODES			18. SUBJECT TERMS (Continue on reverse if necessary and identify by block number)
FIELD	GROUP	SUB-GROUP	
09	03		Microwave Tubes; Coupled Cavity Circuits; Traveling Wave Devices; Computer Simulation Code

19. ABSTRACT (Continue on reverse if necessary and identify by block number)

The problems encountered in the design of circuits for traveling wave devices are of sufficient difficulty that analytic solutions are not usually possible. Historically, resistive networks, electrolytic tanks, and analog computers have been used to simulate devices and thereby permit direct measurement of the field variations. With the advent of large digital computers, it has become possible to solve these problems in a much more general fashion by numerically integrating the fundamental differential equations over a discrete mesh. The recent development of numerical techniques to efficiently handle the massive data storage problem necessary to self-consistently solve Maxwell's equations with sources, combined with the continuing improvement in computer price/performance ratios, has led to the development of computer codes powerful enough to perform three-dimensional "numerical experiments." Codes of this type have been used for a number of years in EMP calculations and in plasma physics. This paper will present the initial results of applying a three-dimensional plasma

20. DISTRIBUTION / AVAILABILITY OF ABSTRACT ☒ UNCLASSIFIED/UNLIMITED ☐ SAME AS RPT ☐ DTIC USERS	21 ABSTRACT SECURITY CLASSIFICATION UNCLASSIFIED
22a. NAME OF RESPONSIBLE INDIVIDUAL ANDREW E. CHROSTOWSKI	22b TELEPHONE (Include Area Code) (315) 330-4381 22c. OFFICE SYMBOL RADC (OCTP)

DD FORM 1473, 84 MAR 83 APR edition may be used until exhausted
All other editions are obsolete

SECURITY CLASSIFICATION OF THIS PAGE
UNCLASSIFIED

simulation code to microwave tube design problems; specifically, the cold testing of coupled-cavity circuits to find phase/frequency characteristics.

ACKNOWLEDGMENTS

The author is grateful to Dr. J. M. Baird at the University of Utah for many helpful suggestions and clarifying discussions. The assistance of Dr. R. H. Jackson, of Mission Research Corporation, in applying the code to this particular problem was invaluable. Finally, the author wishes to thank Litton Systems, Inc., Electron Devices Division, and the U. S. Air Force, Rome Air Development Center, for their joint sponsorship of this project through the AFTER Program contract F30602-82-C-0161 at the University of Utah.

TABLE OF CONTENTS

CHAPTER I

INTRODUCTION

Various methods have been attempted to predict the cold circuit characteristics of coupled cavity circuits for traveling wave tubes. These methods include approximate field analyses [1] and lumped element equivalent circuits [2]. None of these methods can predict the circuit characteristics to a high degree of accuracy. The result is that the circuit design procedure includes physically building and measuring a "first-cut" circuit, and making modifications to obtain the final product. These modifications include both engineering and machining costs.

With the advent of large digital computers with low price/performance ratios, and the development of numerical techniques for efficiently handling the massive amounts of data storage necessary for self-consistently solving Maxwell's equations with sources, it has become financially feasible to make use of computer codes which perform three-dimensional "numerical experiments." Codes of this type have been used for a number of years in Plasma Physics, and particularly for EMP calculations.

This study makes use of a three-dimensional plasma simulation code called SOS (Self-Optimized Sector) [3], developed by Mission Research Corporation. By making certain modifications to the source models and using the output data of the code as input to a Fast Fourier Transform routine, it was possible to perform numerically the resonance tests by which a circuit's Brillouin plot is typically found.

Chapter II will introduce the code and its method, which is a great contrast to the eigenvalue approach used in codes such as Superfish [4]. Chapter III discusses the various source methods which were used. In Chapter IV various test cases are discussed which establish the validity of the method. Chapter V gives the results of a staggered-slot, coupled cavity circuit, and compares these to measured values. The problem of resolution and an apparant numerical instability are discussed in Chapter VI, with an eye towards cost effectiveness. Chapter VII gives a summary of results and recommendations for further study. In Appendix A, the second order accuracy of the non-uniform grid, centered difference derivative method is proved. Appendix B gives a derivation of the Discrete Fourier Transform pair. The equations necessary for fitting a cubic least squares with boundary conditions (zero first derivative) are developed in Appendix C.

CHAPTER II

THE COMPUTER CODE

The SOS (Self-Optimized Sector) code [3] is a fully three-dimensional, electromagnetic, simulation code designed for applications in plasma physics involving charged particles and electromagnetic waves. SOS solves the time-dependent Maxwell equations in finite difference form and uses particle-in-cell (PIC) methods to compute current density sources. Particle trajectories are computed using the relativistic equations of motion. The code was originally developed to run on the CDC Cyber 176. Later revisions have been made to the code to allow it to function on the Cray-1 and the DEC 11/780 (VAX) computers. This project was performed entirely on a DEC machine.

This study dealt only with the "cold-test" of a coupled-cavity circuit, so we need only concern ourselves with the electromagnetic part of the code.

Maxwell's equations are

$$\nabla \times \overline{E} = -\frac{\partial \overline{B}}{\partial t} \qquad \nabla \times \overline{H} = \frac{\partial \overline{D}}{\partial t} + \overline{J} \tag{1}$$

$$\nabla \cdot \overline{B} = 0 \qquad \nabla \cdot \overline{D} = \rho$$

The first two of these completely define the temporal evolution of the fields. The second two may be viewed as initial conditions since they deal with conservation of magnetic and electric charge, which, if satisfied initially, will be satisfied by all subsequent fields generated by the first two equations.

In component form, the two curl equations become

$$\begin{aligned}
\partial_t E_1 &= -\varepsilon_0^{-1} J_1 + (\mu_0 \varepsilon_0 h_2 h_3)^{-1} \{\partial_2(h_3 B_3) - \partial_3(h_2 B_2)\} \\
\partial_t E_2 &= -\partial_0^{-1} J_2 + (\mu_0 \varepsilon_0 h_3 h_1)^{-1} \{\partial_3(h_1 B_1) - \partial_1(h_3 B_3)\} \\
\partial_t E_3 &= -\varepsilon_0^{-1} J_3 + (\mu_0 \varepsilon_0 h_1 h_2)^{-1} \{\partial_1(h_2 B_2) - \partial_2(h_1 B_1)\} \qquad (2) \\
\partial_t B_1 &= -(h_2 h_3)^{-1} \{\partial_2(h_3 E_3) - \partial_3(h_2 E_2)\} \\
\partial_t B_2 &= -(h_3 h_1)^{-1} \{\partial_3(h_1 E_1) - \partial_1(h_3 E_3)\} \\
\partial_t B_3 &= -(h_1 h_2)^{-1} \{\partial_1(h_2 E_2) - \partial_2(h_1 E_1)\}
\end{aligned}$$

Where ∂_i denotes the partial derivative with respect to the i^{th} coordinate, and the coefficients, h_i, are the differential length elements in the coordinate system of interest, e.g.

in rectangular coordinates:	$h_1=1;\ h_2=1;\ h_3=1$
in cylindrical:	$h_1=1;\ h_2=r;\ h_3=1$
and in spherical:	$h_1=1;\ h_2=r,\ h_3=r\sin\theta$.

One can apply various finite difference schemes to these equations based on accuracy, convergence, and cost considerations. SOS contains four finite differencing algorithms from which the most appropriate for a given application may be chosen. Of these, two deal with regions of temporally and spatially varying conductivity and need not be considered for our application. A third algorithm uses the centered difference formula for the spatial derivatives, but is implicit in the time domain of the magnetic field. That is, a "guess" at the future value of the magnetic field is used to calculate the current electric field. This electric field is then used to calculate the next magnetic field value which is compared to the guess. By adjusting the guess appropriately, the algorithm

converges to the desired field values. The fourth method is a straightforward centered difference. In this approach, the electric field is found exclusively from the previously calculated magnetic field values. It is therefore explicit so that no iterative procedure is needed.

Although the third approach will yield more accurate results, it is clearly a more expensive method. For this reason, the explicit, centered difference algorithm was used for calculations in this report. This method can be shown (see Appendix A) to yield second order accuracy to the true derivative, while retaining a fairly flexible grid spacing requirement.

SOS contains the option to sample any of the field components at a fixed point in space as a function of time. This is accomplished by reading the field amplitude at discrete points in time of fixed interval, and writing the result to an output file. It is straightforward then, to apply a Fourier Transform to this data so as to obtain the frequency characteristics of the device under test. To this end, we introduce the Discrete Fourier Transform pair [5]

$$E(m) = \sum_{n=0}^{N-1} \varepsilon(n)\, e^{-j(2n\pi/N)m} \qquad m=0,\ 1,\ 2,\ \ldots,\ N-1$$

$$\varepsilon(n) = \sum_{m=0}^{N-1} E(m) e^{-j(2m\pi/N)n} \qquad n=0,\ 1,\ 2,\ \ldots,\ N-1$$

where N is the number of samples taken. (See Appendix B for a derivation of the DFT pair.)

If we define t_o as the sampling interval, then we have

$$t = \frac{mt_o}{N} \qquad \text{and} \qquad f = \frac{n}{Nt_o}$$

Notice that Nt_o is the total time through which the fields have been tracked in our numerical experiment.

The cost (CPU time) of a simulation is determined primarily by two factors: the number of grid points, and the number of time steps. Obviously, we want to minimize both in order to keep the cost down. The first is limited by the requirement to fully define the physical details (e.g. corners) of the structure. The number of time steps is more complicated, as it is a function of several factors.

The spacing in frequency space is determined by the total time of the run, i.e.

$$f_o = \frac{1}{Nt_o}$$

Therefore, for a desired value of f_o, we can keep N small by making t_o large. However, in order to have stability, t_o is bounded by the Courant Stability Criterion [6]

$$\left(\frac{1}{Ct_o}\right)^2 > \sum_{i=1}^{3}\left(\frac{1}{h_i \delta x_i}\right)^2$$

where the h_i are the coefficients of the differential length elements defined above, and the δx_i are the differential length elements. For example, in cylindrical coordinates

$$\left(\frac{1}{Ct_o}\right)^2 > \left(\frac{1}{\delta r}\right)^2 + \left(\frac{1}{r\delta\theta}\right)^2 + \left(\frac{1}{\delta z}\right)^2$$

or

$$t_o < \frac{1}{C}\left[\left(\frac{1}{\delta r}\right)^2 + \left(\frac{1}{r\delta\theta}\right)^2 + \left(\frac{1}{\delta z}\right)^2\right]^{-\frac{1}{2}}$$

The final factor to be considered is that in order to use a Fast Fourier Transform, f_o and t_o must be chosen so that N is an integer power of two. This last consideration did not pose any problem in this study because if the "power of two" restriction was inconvenient, the FFT could be replaced by a Discrete Fourier Transform (not fast). The extra cost incurred by this change was insignificant in comparison to the cost of running the plasma simulation.

CHAPTER III
SOURCE CONFIGURATION

The sources available in the code (SOS) were not suitable for our purposes, so the approach used was to manipulate one component of the electric field at various points in space. This was accomplished by adding the desired source (e.g. a point source oscillating at a desired frequency, or a point impulse function) to the existing field value as a "correction" term.

This approach allowed for a good deal of freedom in coupling to the desired resonance. In fact, it was possible to change the coupling separately in physical and frequency space. By using an impulse as the source, all frequencies were excited. If the impulse was tailored in space to fit the desired field pattern (which is known in the case of a simple cavity) then the code no longer sees this as an impulse, but rather as initial conditions. This is because we are using the algorithm (see Chapter II) which is explicit, and our source is being artificially added to the existing fields. When we adjust the field values at all points in the volume simultaneously to exactly match one mode, then there are no steps in the field in physical space, and the code does not see the step in time, but rather treats it as if that mode had always been there and we get a single spike in the frequency spectrum.

Regardless of what type of source is used, the energy going into the system will try to resonate in the natural modes of the system. Most

of the energy, in fact, should go into the natural mode which we are the closest to, with respect to frequency and field shape.

Since the field shape is known exactly in a simple cavity, and approximately in a reentrant cavity, initial conditions proved to be a good way to find the primary resonance. Having a source point oscillating at a frequency close to the desired resonance also provided good results.

Figures 3.1 and 3.2 show the frequency spectrum of a simple and reentrant cavity, respectively, in which a point source oscillating at a frequency close to the primary resonance was placed. Notice that the shape of the curve in each case is basically that of a peak at the primary resonance, with the source and higher order resonances superimposed upon it. Figure 3.3 shows the spectrum, after a beam hole was introduced. Notice that now the shape of the curve has changed significantly and there is energy at zero frequency which is comparable to the amount at the primary resonance. After introducing the slot, while still using a point source, Figure 3.4 shows the zero frequency amplitude to be considerably above the primary resonance. In this latter case, if we look at higher frequencies, as in Figure 3.5, we see that the code is predicting an incredible amount of energy going into some higher order mode (about 46 GHz). This high frequency problem is not true for the "no-slot" case, as shown in Figure 3.6.

From these figures, it is evident that the predicted spectrum is not physically realistic for either the case of a half-cavity with a beam hole, or a half-cavity with a beam hole and 80^0 slot. Three possible methods of improving the simulation come to mind immediately. First, the number of grid points might be increased to improve the accuracy of numerical

derivatives. Second, the source might be placed at the resonant frequency (i.e. improve the coupling in frequency space). Finally, the source might be tailored to fit the field shape of the desired mode (i.e. improve the coupling in physical space).

The first suggestion, improving the grid, did change the results, but did not solve the problems mentioned above. This can be seen by comparing Figure 3.7 to Figure 3.5. The second suggestion amounts to knowing the solution to find the solution, so it is not usable. The third idea is useful, because we know the desired mode has a concentration of electric field across the ferrules, so it seemed reasonable to change from a single point source to a ring of sources located at all grid points between the ferrules. This method solved the anomaly of having large amplitude at zero frequency, as shown in Figures 3.8 and 3.9. However, it did not solve the high frequency problem for the cavity with a slot, as shown in Figure 3.9.

With these improved results, it seemed good to observe the effect of our other two suggestions. Figures 3.10 and 3.11, with a finer grid, may be compared to Figures 3.8 and 3.9. Figures 3.12 and 3.13, in which the source is placed at the resonant frequency, may be compared with Figures 3.8 and 3.9. In each case, the change does not affect the result of interest, which is the detection of the primary resonance and its location.

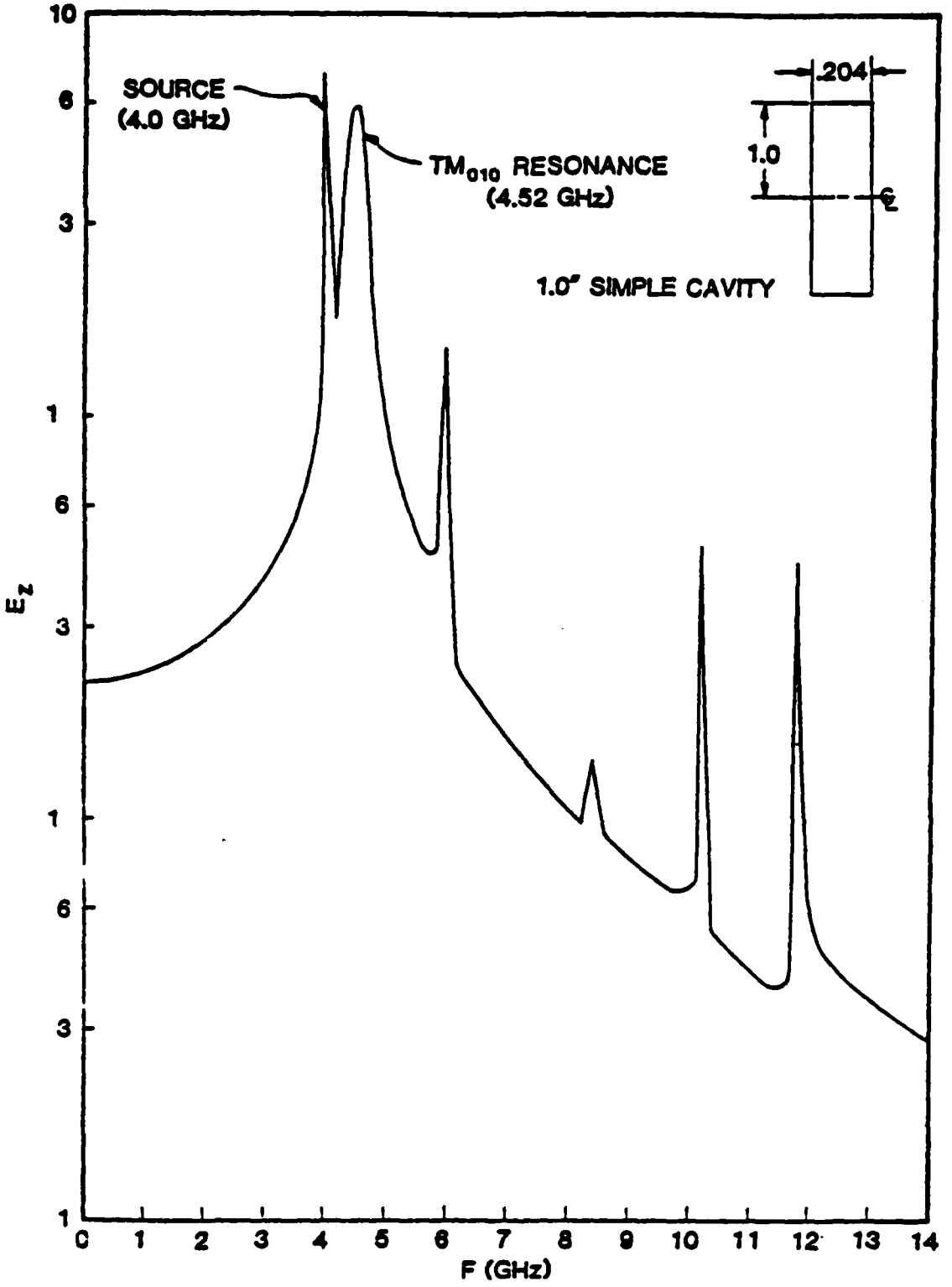

FIGURE 3.1 - Amplitude vs. Frequency in a simulation of a simple cavity in which the source was a point, oscillating just below (in frequency) the primary resonance. Note that the shape of the curve is primarily a peak at the desired resonance, with the source and higher order resonances superimposed upon it. Dimensions are inches.

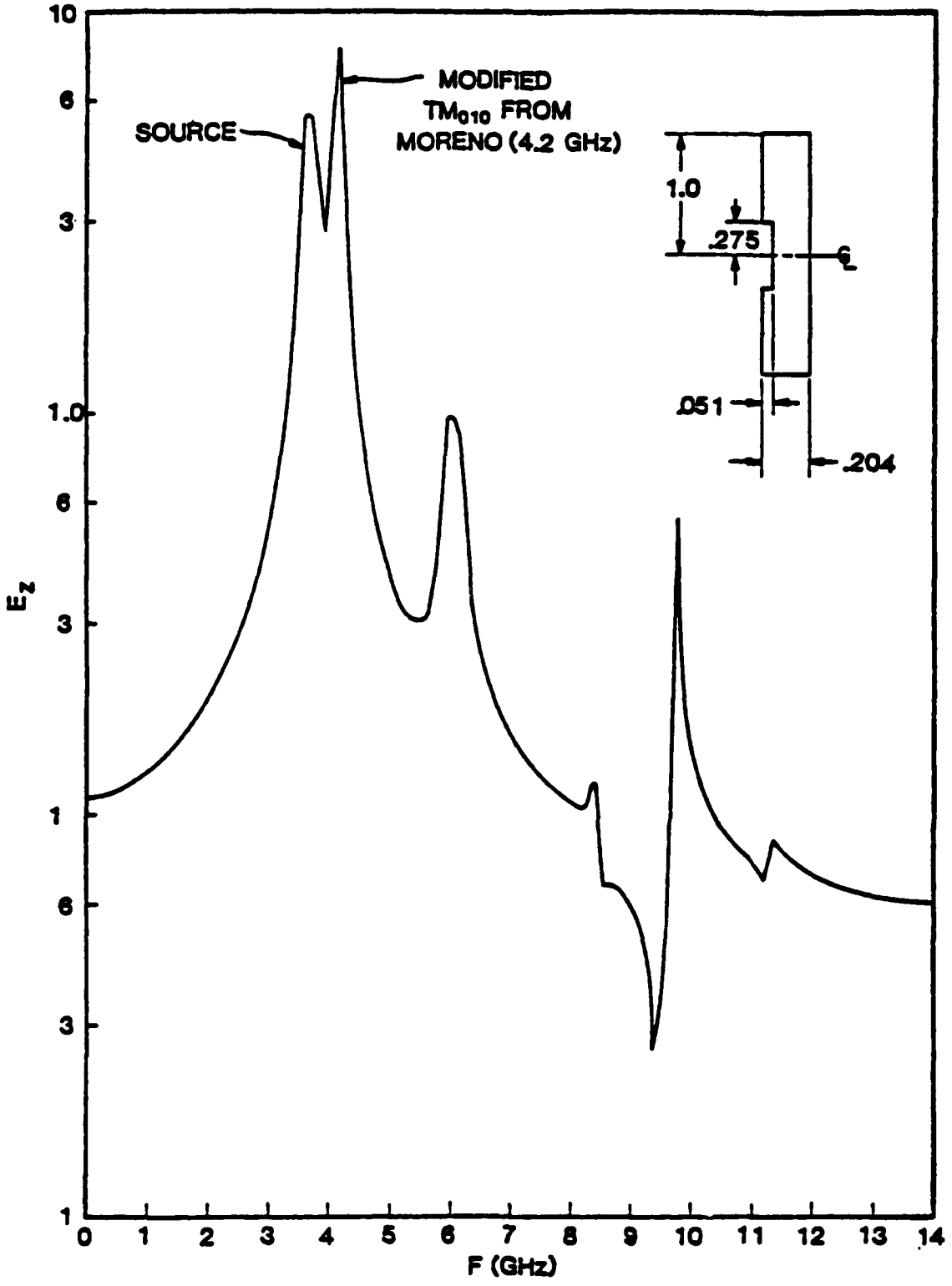

FIGURE 3.2 - Amplitude vs. Frequency in a simulation of a reentrant cavity of indicated dimensions. Again, a point source was placed just below the desired resonance, which was known from Moreno's curves [8]. The curve is not as smooth as in the previous figure, but the primary resonance is predicted by the code to be just where we expect it.

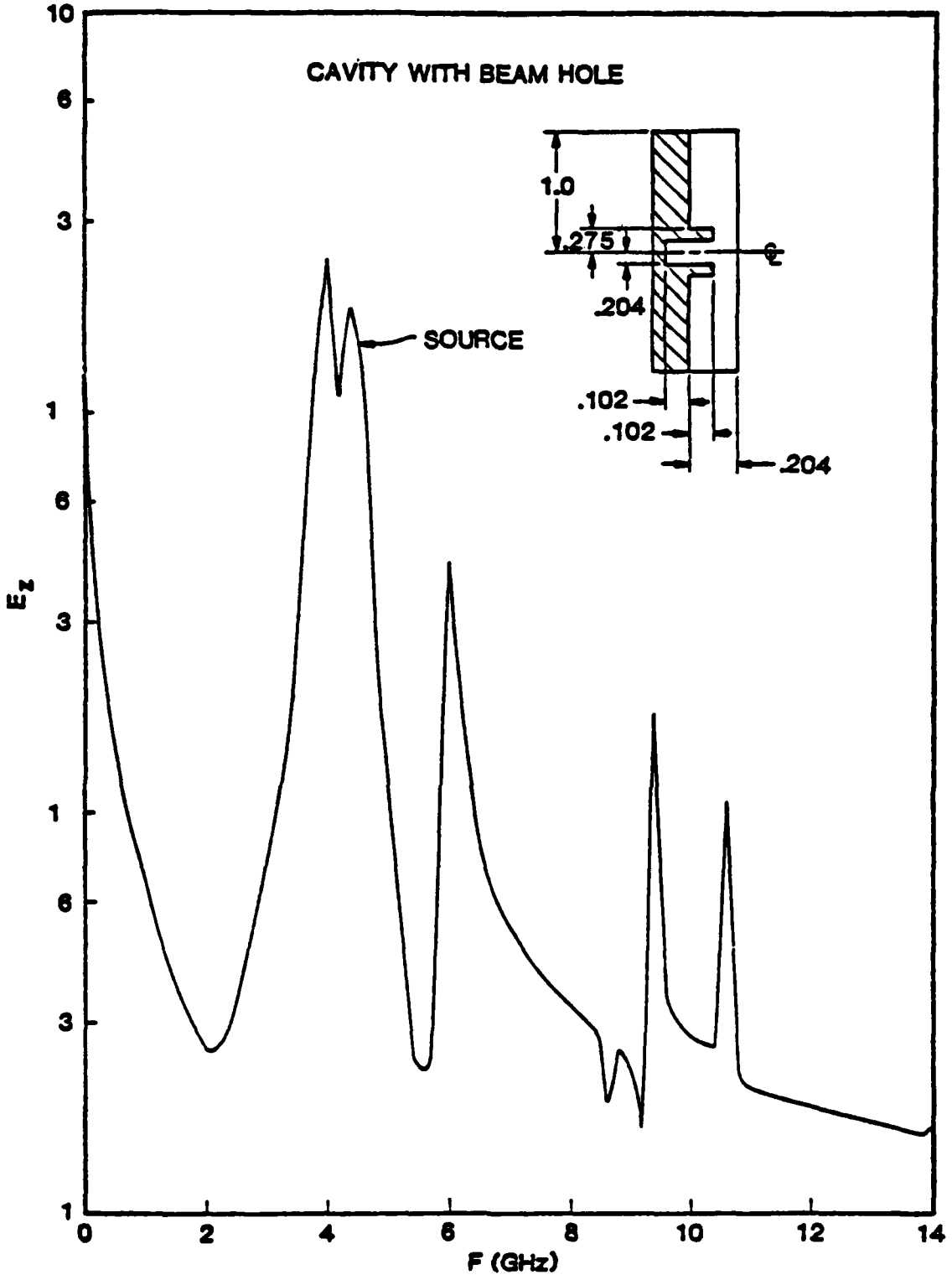

FIGURE 3.3 - A reentrant cavity after the inclusion of a beam hole. The extension of the beam hole is to account for the wall thickness between cavities. In this case, no predicted value for the resonance was available, but as can be seen from the figure, the source was placed slightly above the resonant frequency.

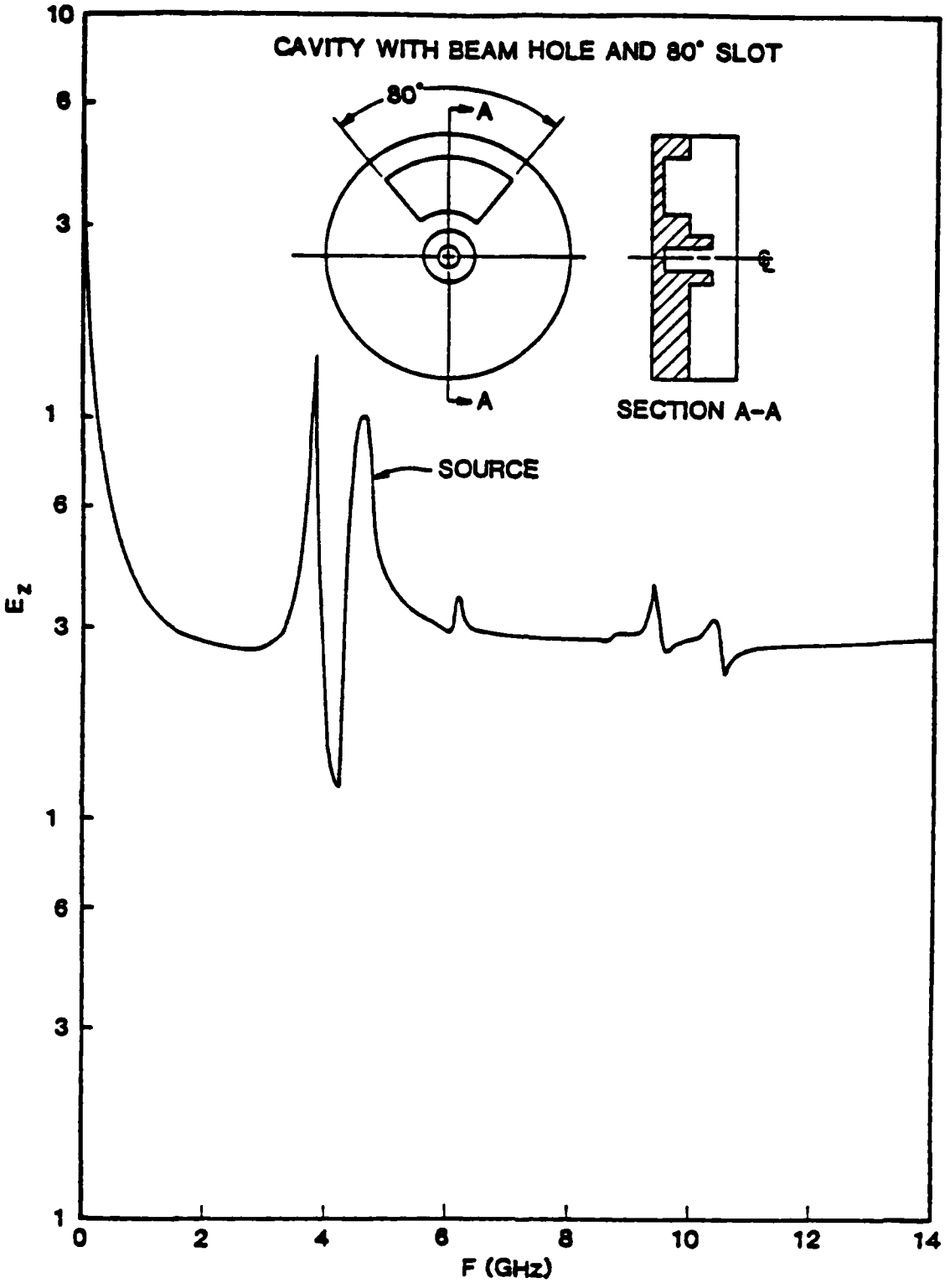

FIGURE 3.4 - The final step to modeling a half cavity is the inclusion of the coupling slot. This lowered the resonant frequency slightly, and changed the overall shape of the curve dramatically. It should be noted that this step makes the problem a truly three-dimensional one.

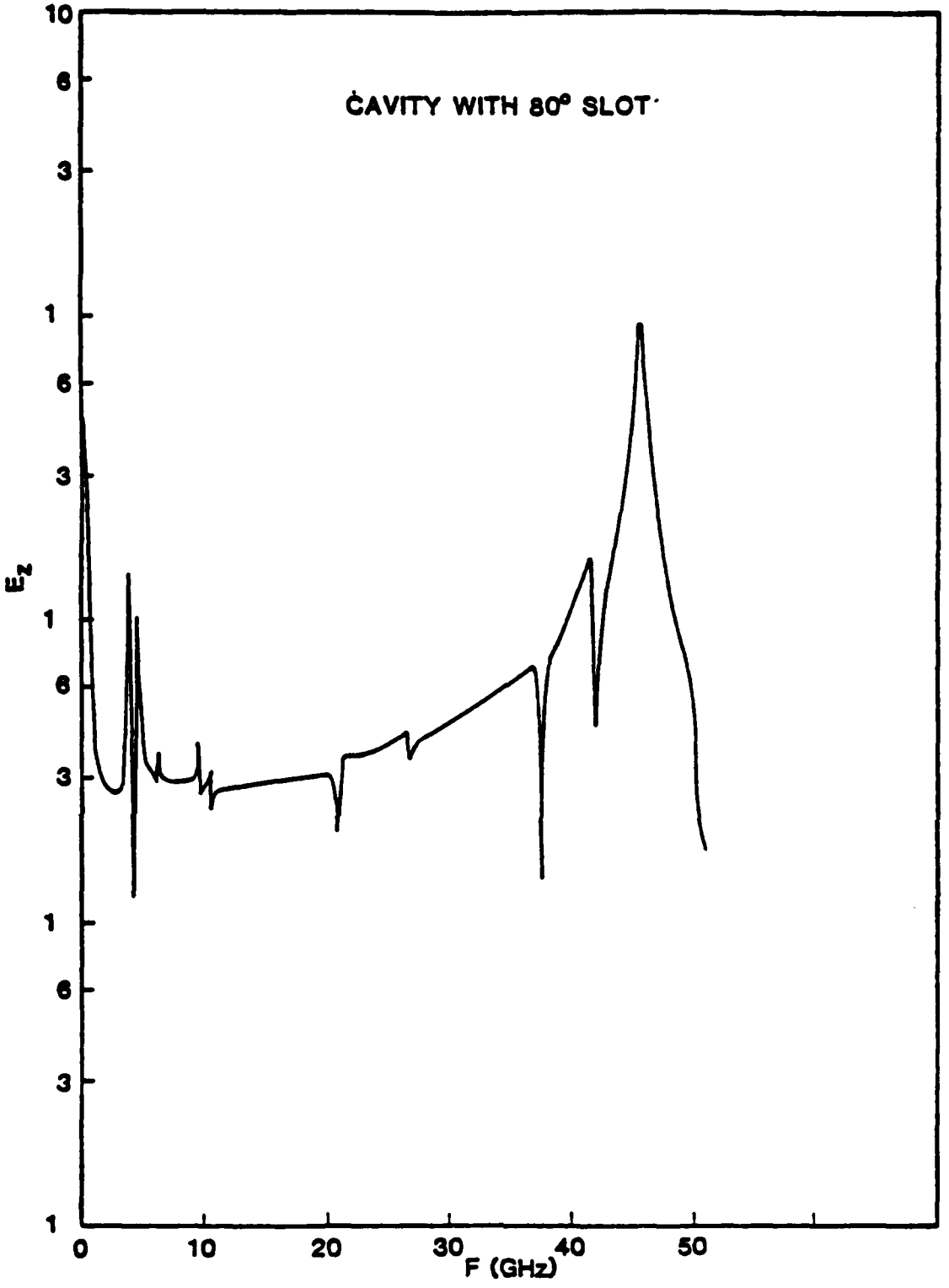

FIGURE 3.5 - This figure is the same as Figure 3.4, but it shows all of the data obtained from the FFT (not just 0-14 GHz as in the previous figure). Two properties of this curve are somewhat disturbing. First the large amplitude at zero frequency, and second the large amplitude at high frequency.

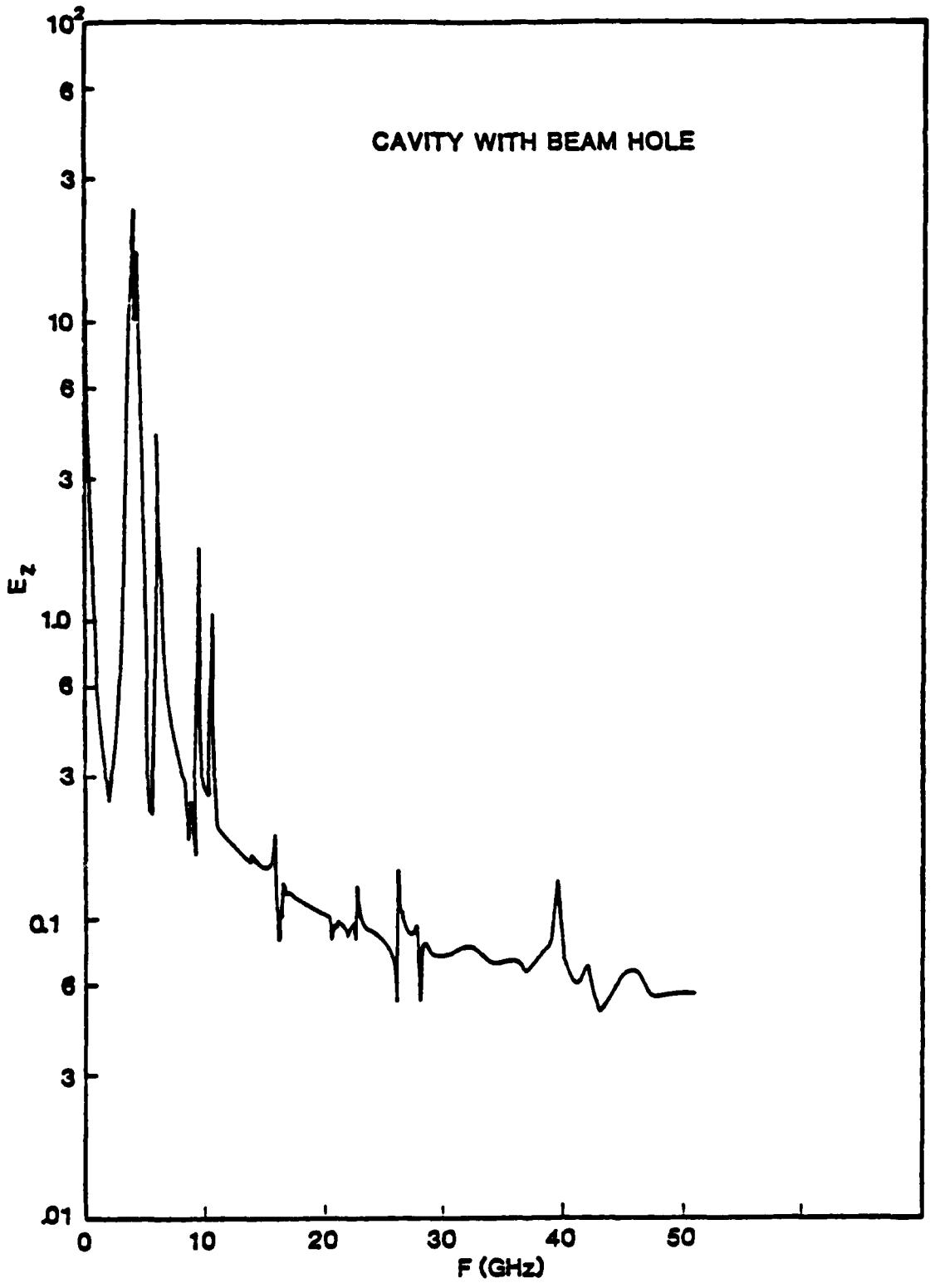

FIGURE 3.6 - Extended view of Figure 3.3. None of the high frequency problem is present here, but the large amplitude at zero frequency is.

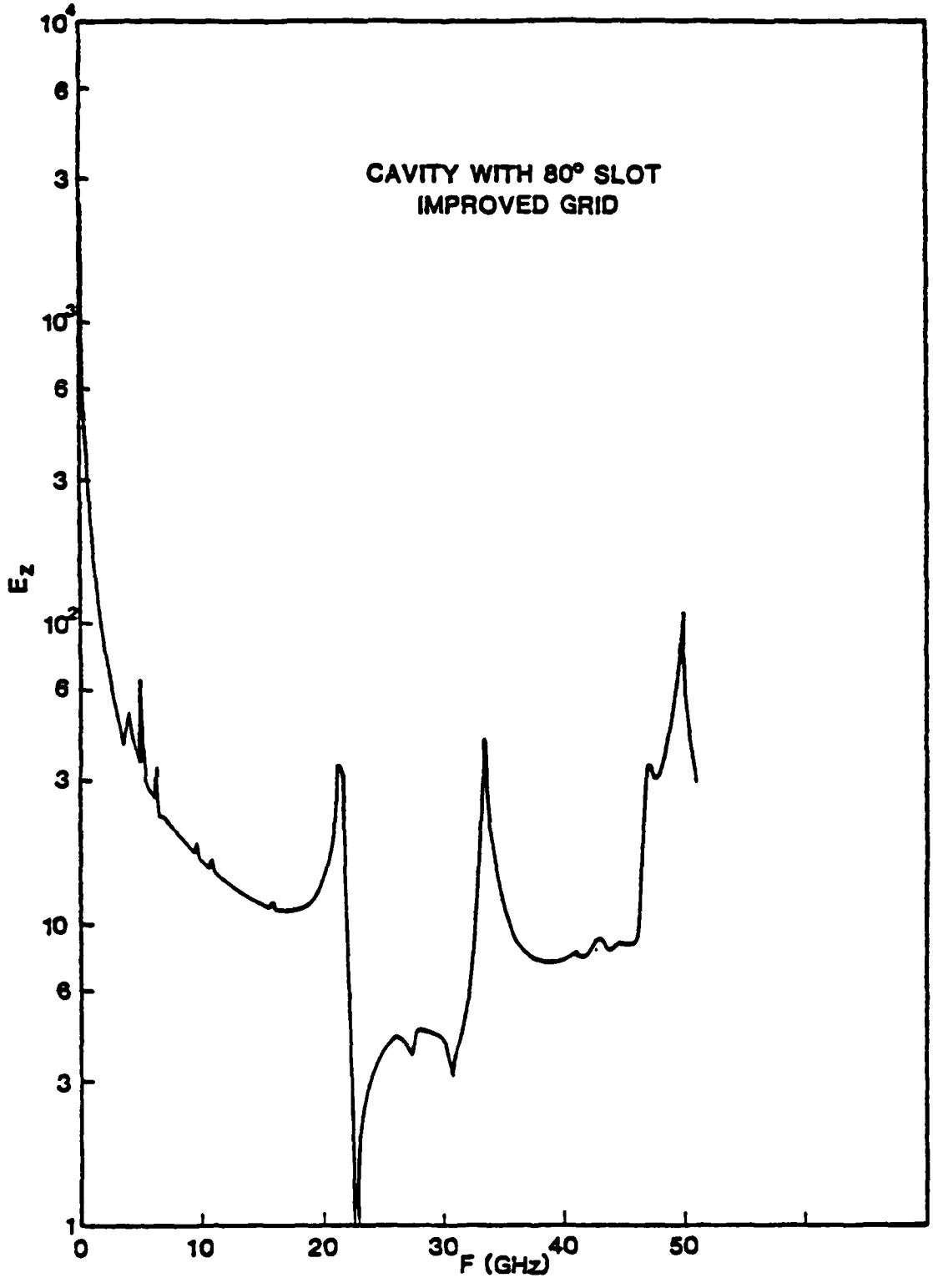

FIGURE 3.7 - This is the same structure that was simulated in Figure 3.5, but with a better grid (i.e. more grid points). Improving the grid has clearly not solved either of our problems, in fact it has made the zero frequency amplitude considerably larger.

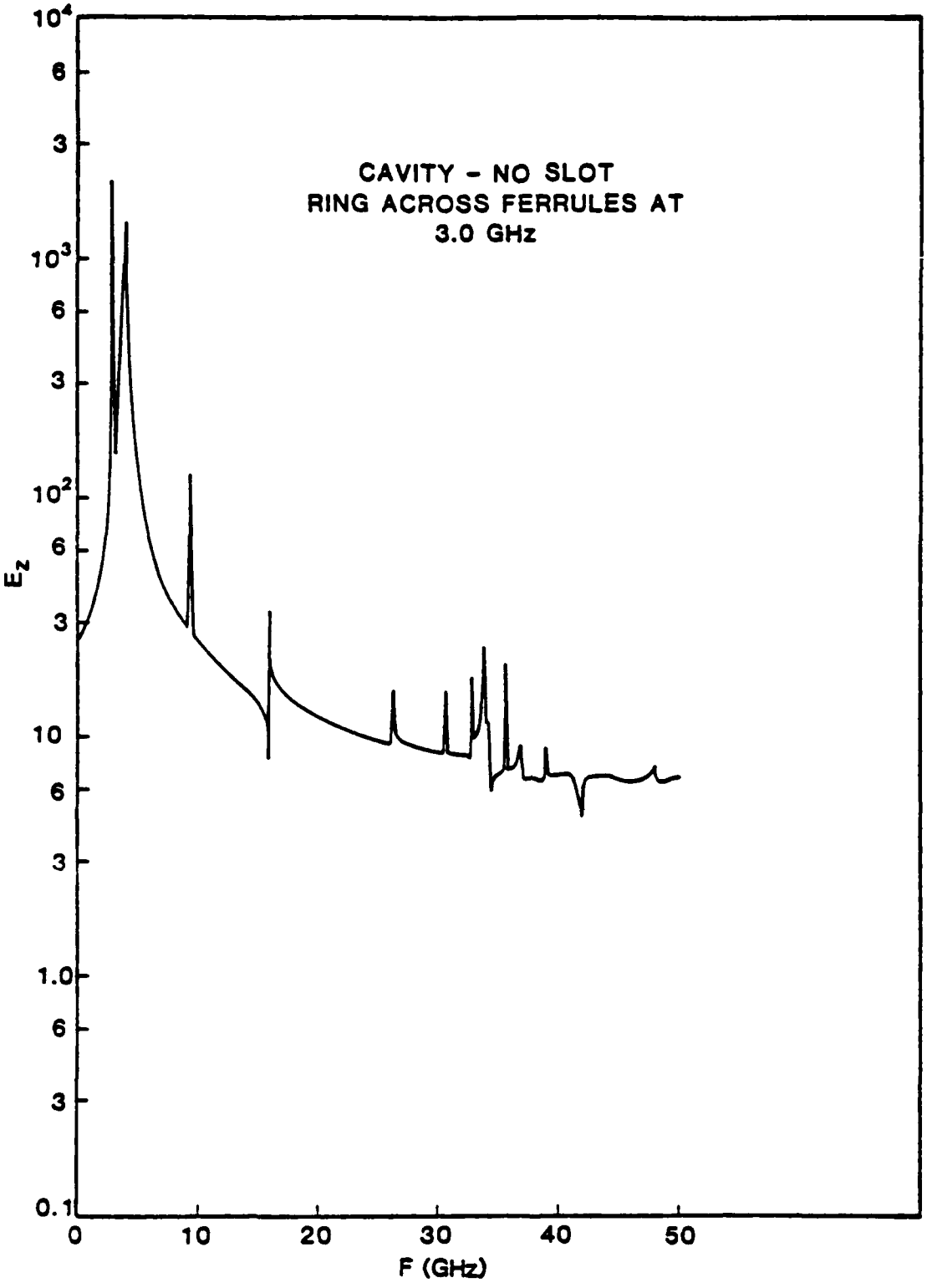

FIGURE 3.8 - By changing the source from a single point to a ring of points in the θ-Z plane corresponding to the ferrule (i.e. improving the coupling to the desired mode in physical space), the zero frequency problem of Figure 3.6 was eliminated.

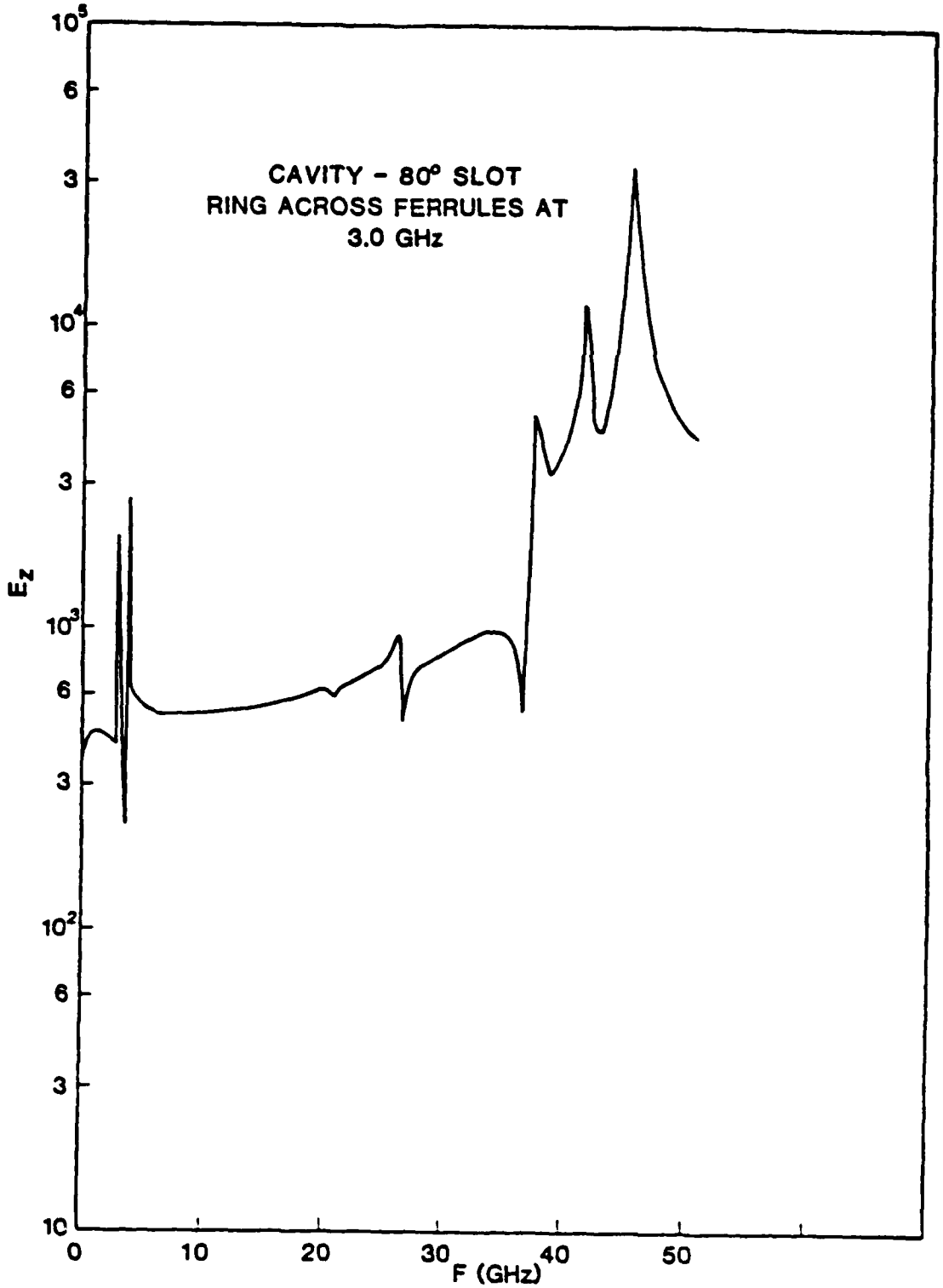

FIGURE 3.9 - With the inclusion of the improved source, the zero frequency amplitude was reduced to a reasonable value for the cavity with the slot. It is evident, however, that this did not help the problem at high frequencies.

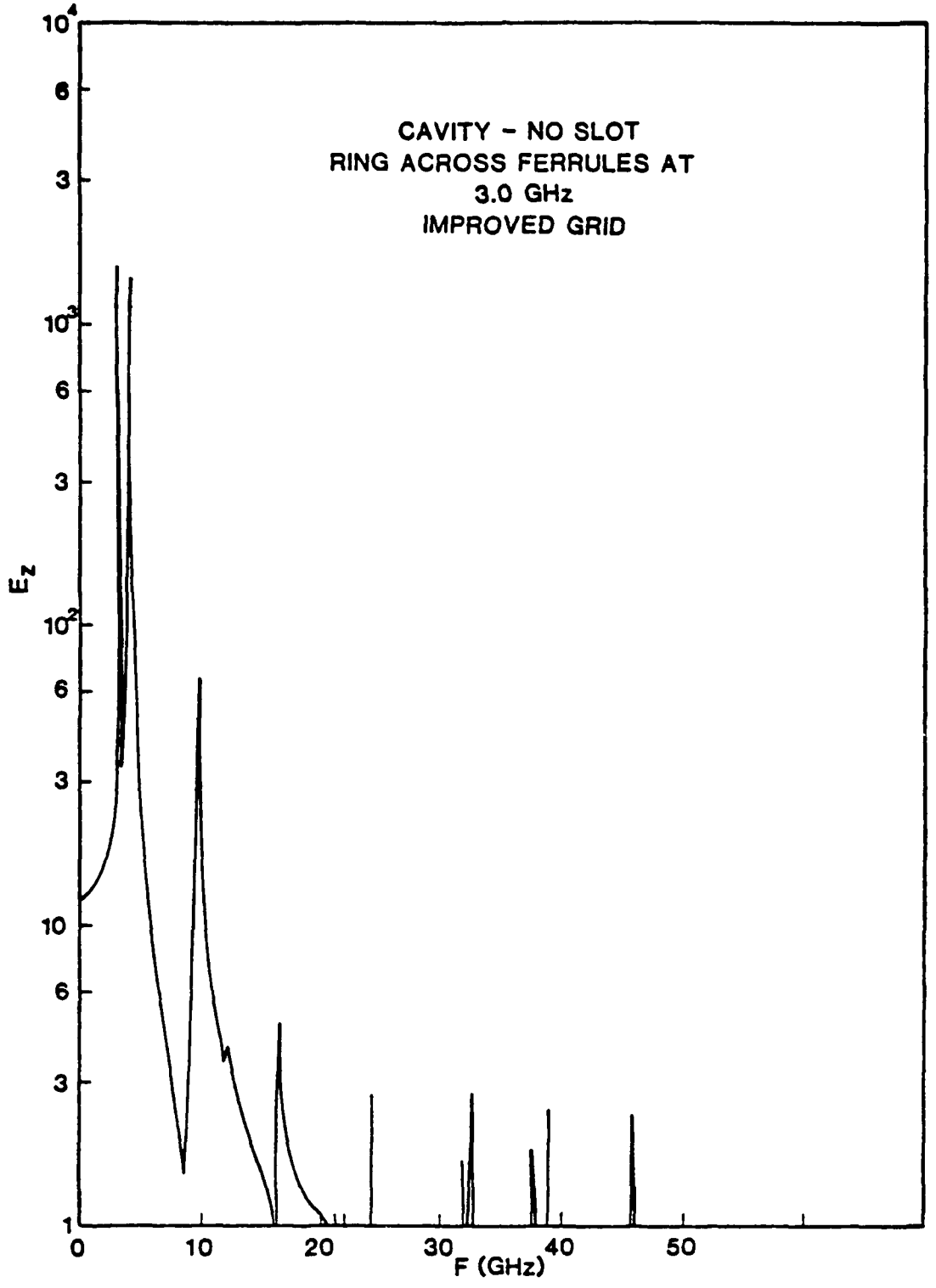

FIGURE 3.10 - By comparing this to Figure 3.8, the results of using a finer grid with the improved physical space coupling may be seen for the cavity with no slot.

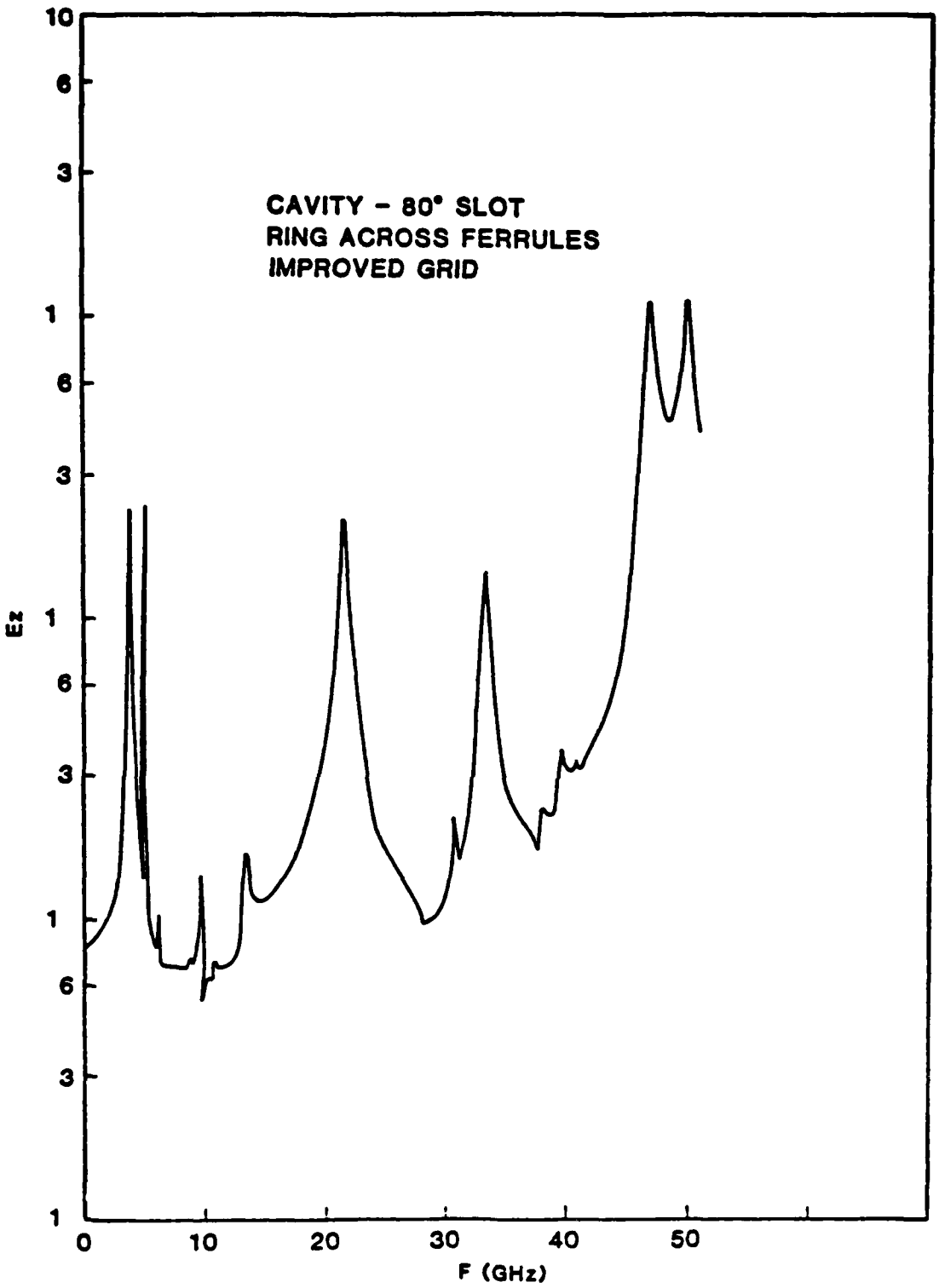

FIGURE 3.11 - This result is a sort of hybrid of Figures 3.7 and 3.9. The ring source at the ferrule has kept the zero frequency amplitude low, as in Figure 3.7, but the improved grid has introduced some other resonances which were evident in Figure 3.9.

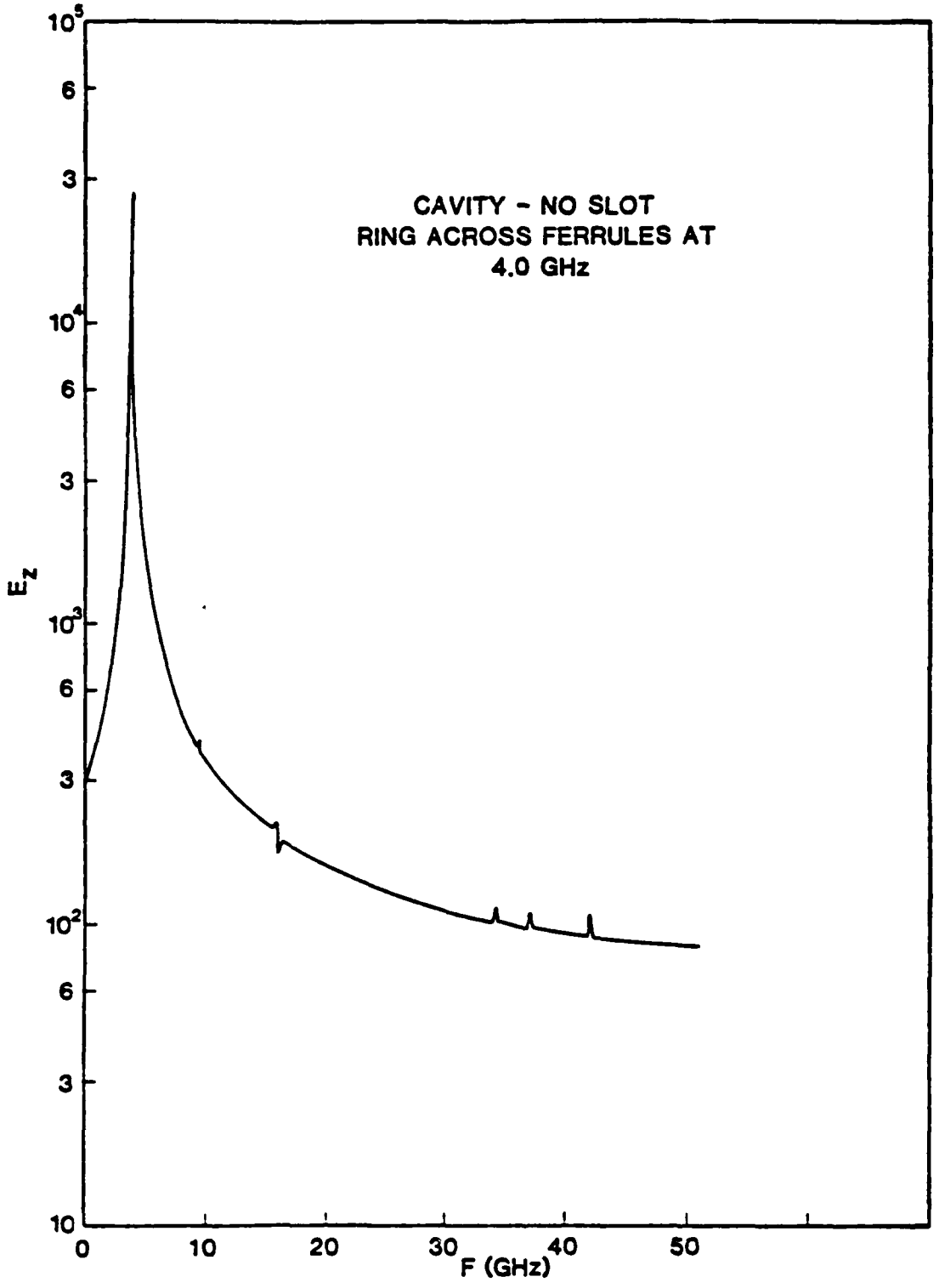

FIGURE 3.12 - Placing the source on the frequency found in Figure 3.8 to be the resonant value, the curve is very clean as one would expect since we are coupling almost perfectly to a single mode.

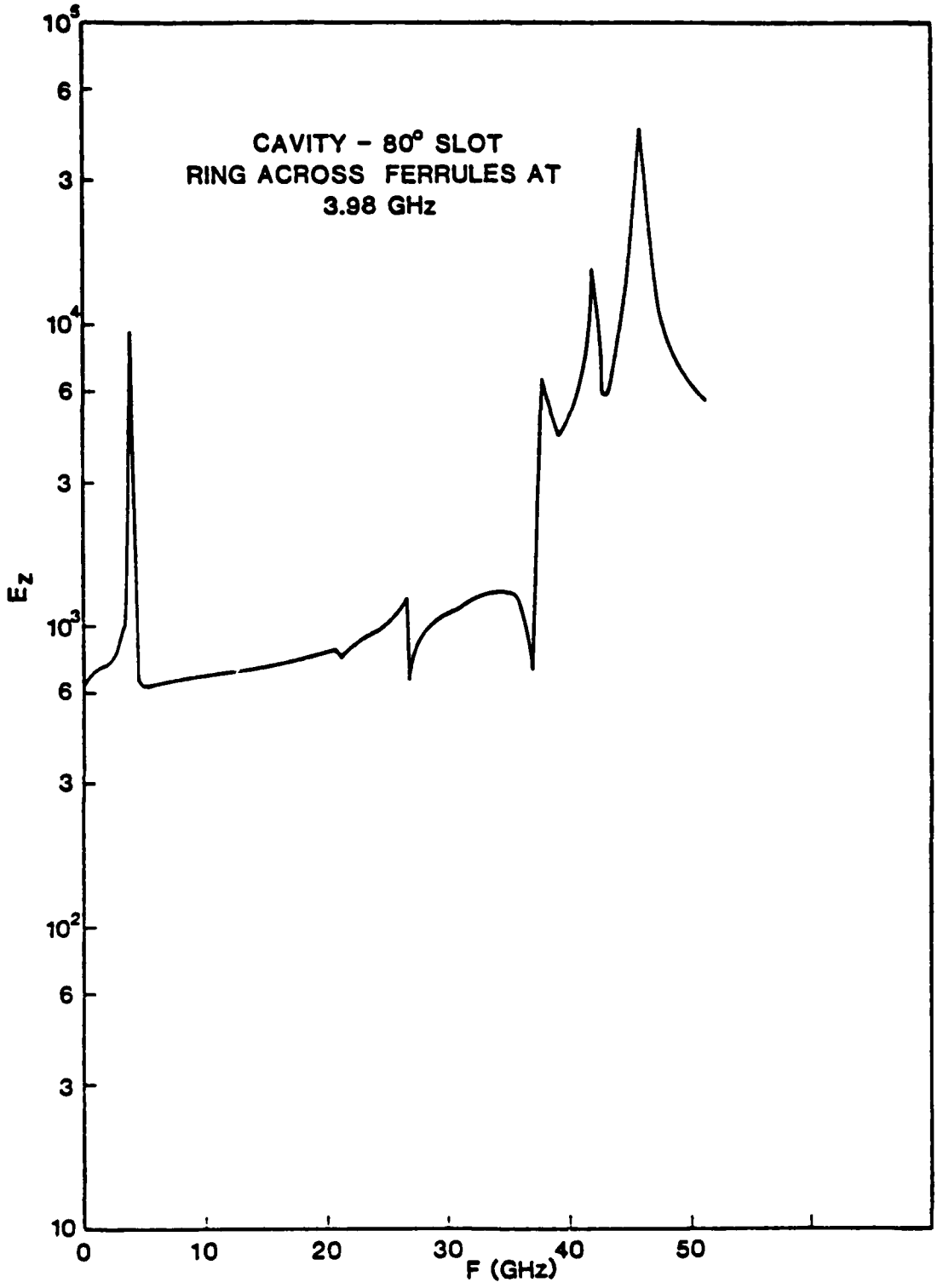

FIGURE 3.13 - Placing the source on the resonance does not have the same effect when our simulation includes a slot. It seems clear that the high frequency problems are a numerical anomaly which are not physically realistic and should not concern us as long as they do not affect our ability to accurately determine the true resonance of our structure.

CHAPTER IV
RESULTS

As illustrated in the previous chapter, the approach used in this project was to check the accuracy of the code (SOS) and the FFT routine against simple test cases, and work towards the desired structure. The obvious choice for a first test case was a right-circular-cylindrical cavity. There are two reasons why this was a good choice. First, the results could easily be compared to the theoretical solution [7], and second, a relatively small number of grid points accurately represented the structure so that test runs on the code were inexpensive.

Accurate results were obtained for the simple cavity case (less than 1% error), so the next logical structure was a reentrant cavity. A reentrant cavity, which had a variable inner conductor height, was available for measurement. The calculated (by SOS) and measured values are shown versus inner conductor height in Figure 4.1. In all cases, the measured value agreed with the value given by Moreno's curves [8] to two digits (which is the limit of accuracy of the curves). The error of the calculated value from the measured value varies from 0.9% at h/L=0 to 4.8% at h/L=5/6. The true error, i.e. between the simulation and the lossless cavity which it simulated, was probably less than indicated by these measured values. The reason for saying this is that the reentrant cavity with h/L=0 is really a simple cavity, and the theoretical resonance was between the calculated and measured values. The calculated value was only in error by 0.2% when compared to the theoretical value at h/L=0.

After inserting a beam hole and a coupling slot, our structure is one half of a coupled cavity, whose resonant frequency is the upper cutoff of our structure. (Actually, this is one half of an "in-line" slot coupled cavity. However, the change in resonant frequency of a single cavity in which the slots were in-line as compared to one in which they were staggered was measured as less than 0.5%.) Figure 4.2 shows the measured and predicted (SOS) resonance values at various stages of cavity development. It is interesting to notice that the accuracy becomes significantly worse when the slot is introduced. This is, in fact, the point at which the problem truly becomes three dimensional (it has up to this point had circular symmetry). It should be pointed out that the predicted values in Figure 4.2 are actually the center point of error bars (for reasons which will be explained in Chapter V), but for clarity only a point is shown at this stage. Although the predicted upper cutoff value is in error by approximately 5% (± uncertainty), we are getting a distinct resonance which encourages us to try to find more points on the Brillouin curve.

Simulations of multiple cavities were performed, which predicted multiple resonances as expected. Two cavities with the grid overlaid are shown in Figure 4.3. Notice the non-uniform grid, as mentioned in Chapter II, and justified in Appendix A. These multiple cavity runs were all done with a ring of source points between the ferrules in one cavity only, oscillating at a frequency below the resonances. Figure 4.4 is the resulting predicted ω-β. The solid lines are drawn through the physically measured values. If the best end of the error bars is taken as the predicted value, then the worst error is about 3%. Taking the worst end

of the error bars, the predicted value is off by 6%. Therefore, the worst error is somewhere between 3 and 6%. Although this is a disappointingly large value for the error in prediction, it does represent a slight improvement in phase velocity prediction over typically used equivalent circuit techniques. In Chapter VI, it is noted that by application of a "least squares" cubic to the data, this error can be significantly reduced. For most applications, the upper and lower cutoff are not the areas of interest. The area in which we would desire the most accuracy would be centered about $\beta p=\pi/2$, say from $\pi/3$ to $2\pi/3$. In this reduced region, using the least squares curve, the error is everywhere less than 1%. This seems to be a very satisfying result.

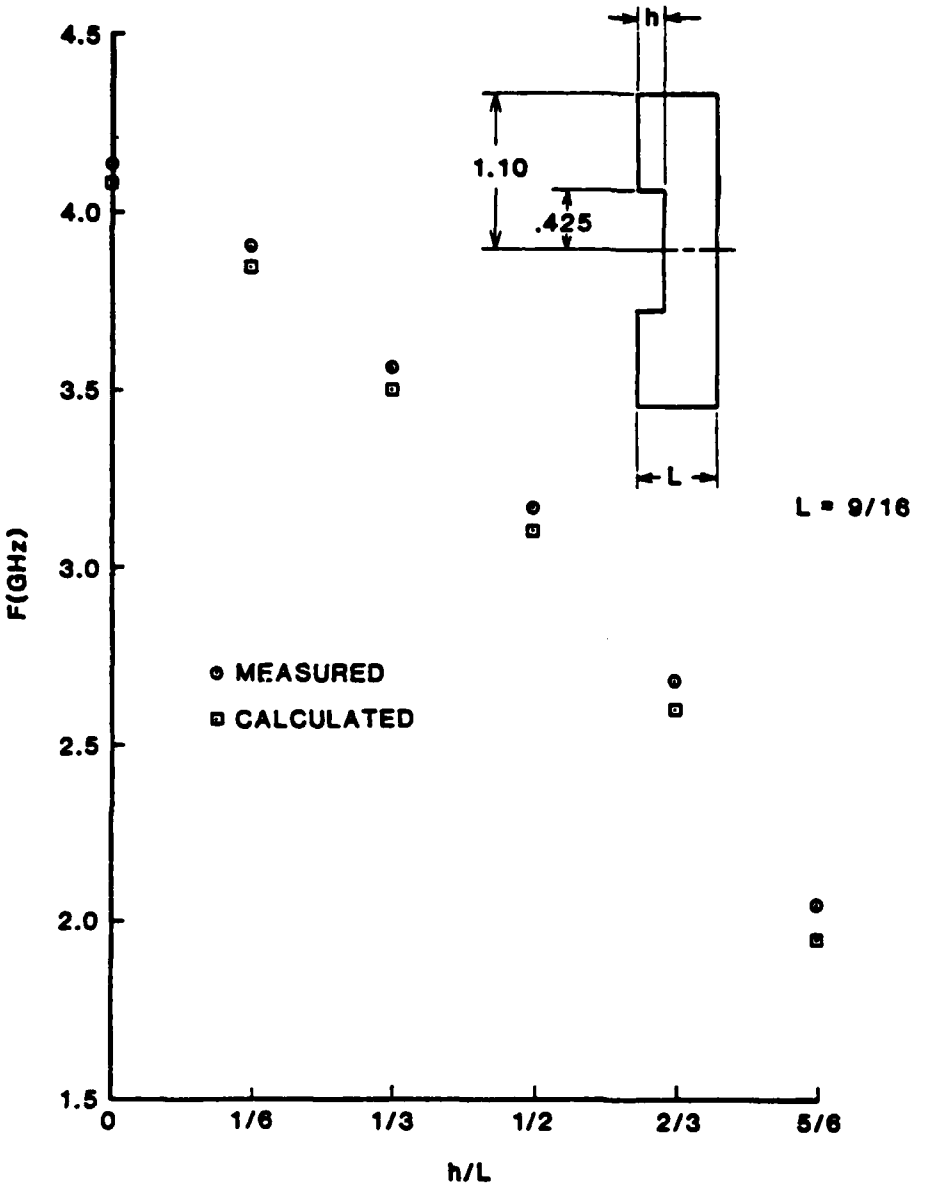

FIGURE 4.1 - Measured and calculated (by the code) resonant frequencies of a reentrant cavity with various values of inner conductor height (h). All dimensions are inches, the two radii and the cavity length are fixed, the inner conductor height being the only variable.

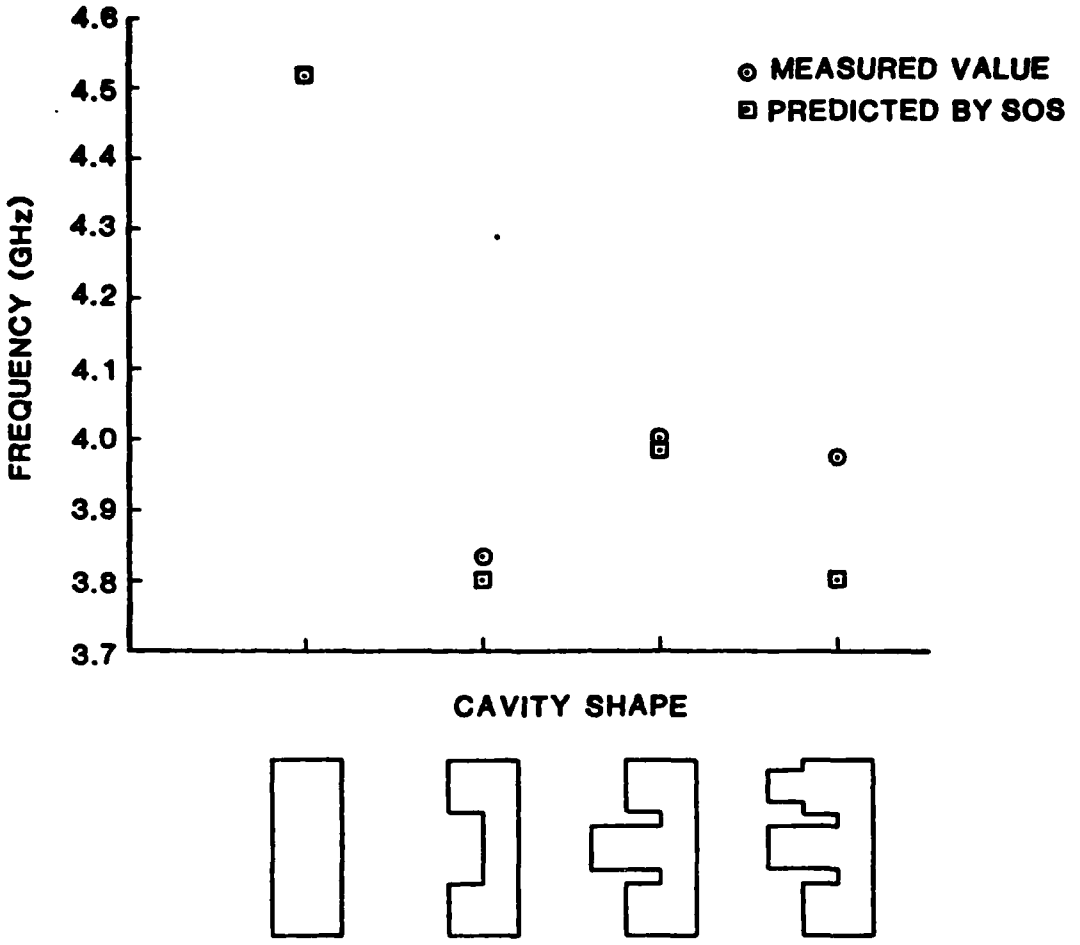

FIGURE 4.2 - Measured and predicted (calculated) values of resonant frequency for the various stages of evolution from a simple cavity to the half "coupled cavity" with beam hole and slot. Even with the sudden increase in error at the inclusion of the slot, the error is still below 5%.

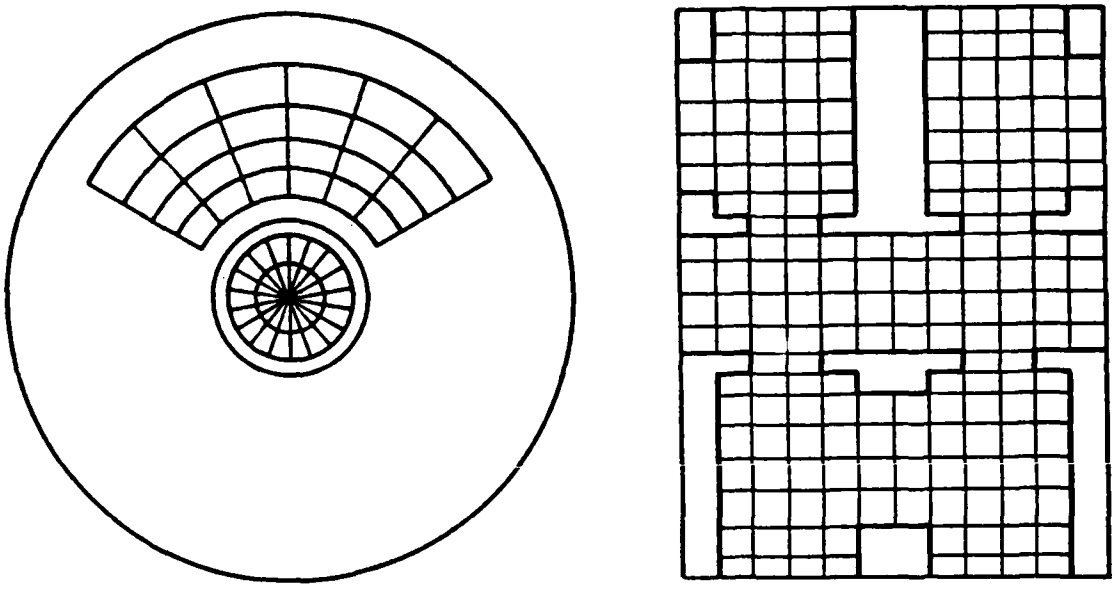

FIGURE 4.3 - Front and cross-section views of a two cavity stack with the grid used in the simulation indicated. Notice that the grid was chosen to be uniform in θ and Z, but non-uniform in r.

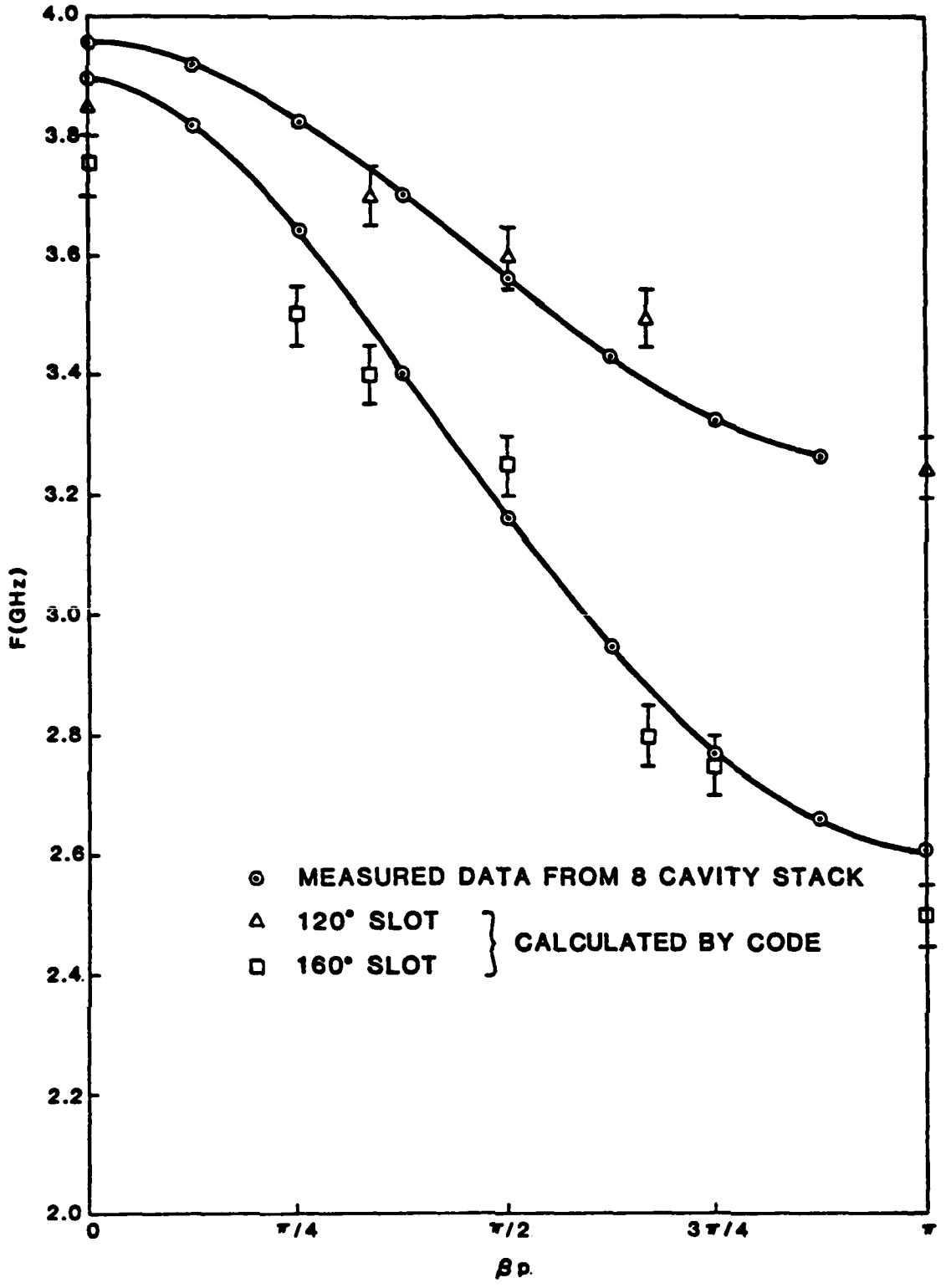

FIGURE 4.4 - The Brillouin plot of coupled-cavity circuits with the indicated coupling slot angle. The calculated values are single data points predicted by a particular run with uncertainty shown by error bars (see Chapter V on resolution).

CHAPTER V
RESOLUTION

Figure 5.1 shows an analog signal which is just resolved by the common 3 dB definition. If discrete samples of the signal are taken, as shown in Figure 5.1, at regular intervals of f_o, where f_o is comparable in magnitude to the width of the peaks, then we see (in Figure 5.2) that the discrete samples are not resolved by the 3 dB definition. Furthermore, we cannot determine from the discrete samples exactly where the peak is located. We can, however, say that the peak is within half the sampling width of the local maximum sample. With these two factors in mind, we have defined in this study a discrete sample to be resolved if there exists a sample which is a local maximum. That is, if the sample is greater than both of its nearest neighbors. Furthermore, we will say that the peak is "resolved to f_o." That is,

$$f_{max} - \frac{f_o}{2} < f_{peak} < f_{max} + \frac{f_o}{2} .$$

We have seen that the spacing in frequency, f_o, is determined by the total run time, Nt_o.

$$f_o = \frac{1}{Nt_o} .$$

Therefore, the total run time should be long enough to resolve the resonances in two ways. First, if more than one resonance is expected, then f_o must be small enough to allow both of the peaks to be local maxima. Second, f_o must be small enough to determine the location of

each peak to reasonable accuracy. One would expect then, that the limiting factor in resolution would be the cost associated with run time.

The limiting factor for this study, turned out to be an instability in the calculations. For an undetermined reason, it was found that the higher frequencies grew in amplitude much faster than the low ones. When these high frequencies became extremely large in amplitude, the lower frequencies (which were in the range of interest) were obscured by them. Figures 5.3 through 5.5 illustrate this problem. In Figure 5.3, the source, at 3.0 GHz, and the lowest resonance, expected just below 4.0 GHz, are not yet resolved due to the large size of the frequency spacing (0.4 GHz). After doubling the run time, Figure 5.4 shows that the source and primary resonance are resolved, but most of the energy is now in the higher frequencies, with the major resonance at about 46 GHz. Figure 5.5 shows that after again doubling the run time, the source and primary resonance are now totally obscured by the resonance at 46 GHz.

Since this instability was one which grew in time, it was possible to perform one long run and take the data for the FFT from time zero up until the instability just obscured our desired results and then truncate all following data. This was the method used to obtain the ω-β plot shown in Chapter V. In order to obtain the data shown there for the 160^0 slot, two runs were performed which modeled three and four cavities, and gathered slightly more data than could be used (due to the instability). These runs were performed at a total cost of less than $150.

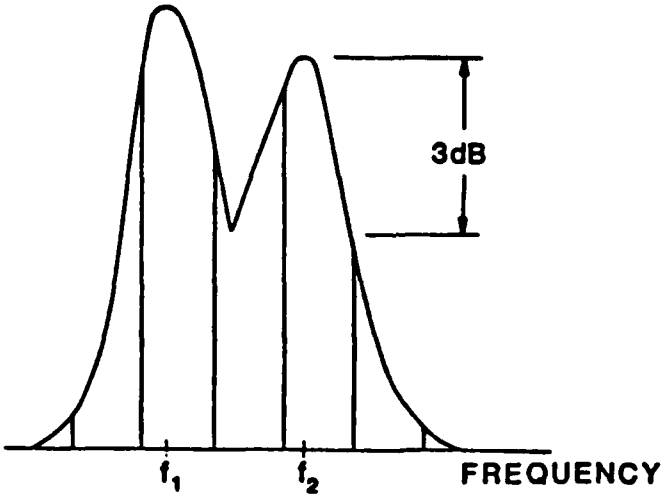

ANALOG SIGNAL WITH DISCRETE SAMPLINGS

FIGURE 5.1 - Discrete samples overlaid on an analog signal with two peaks that are just resolved by the common 3 dB definition.

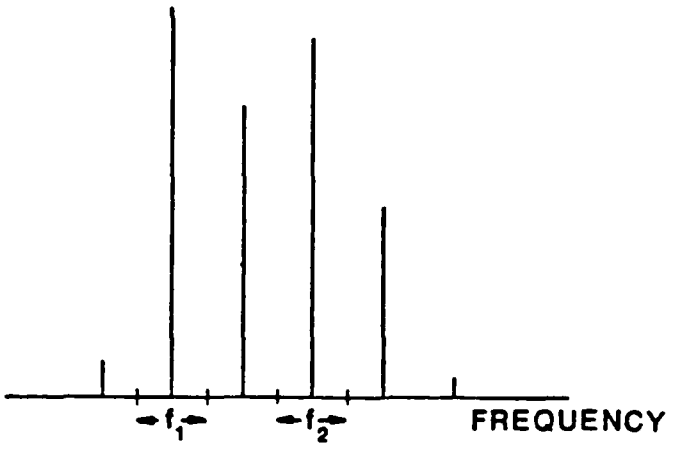

DISCRETE REPRESENTATION OF THE SIGNAL

FIGURE 5.2 - Discrete samples from Figure 5.1. The samples are not resolved by the 3 dB definition, and furthermore, the true location in frequency of the maximum may only be determined to the limits indicated.

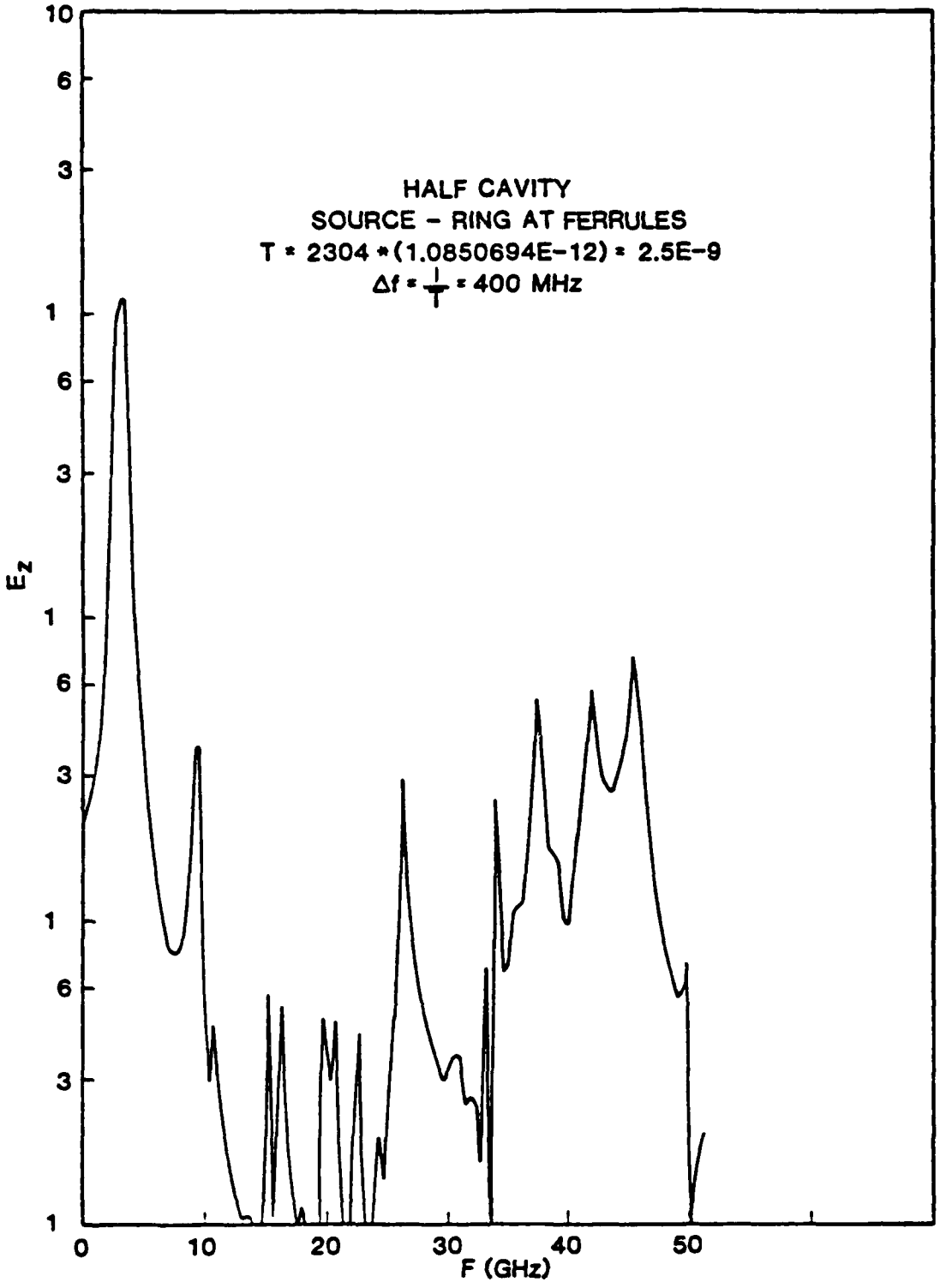

FIGURE 5.3 - Sampling not frequent enough to resolve the source and the primary resonance, which are both contained in the first peak.

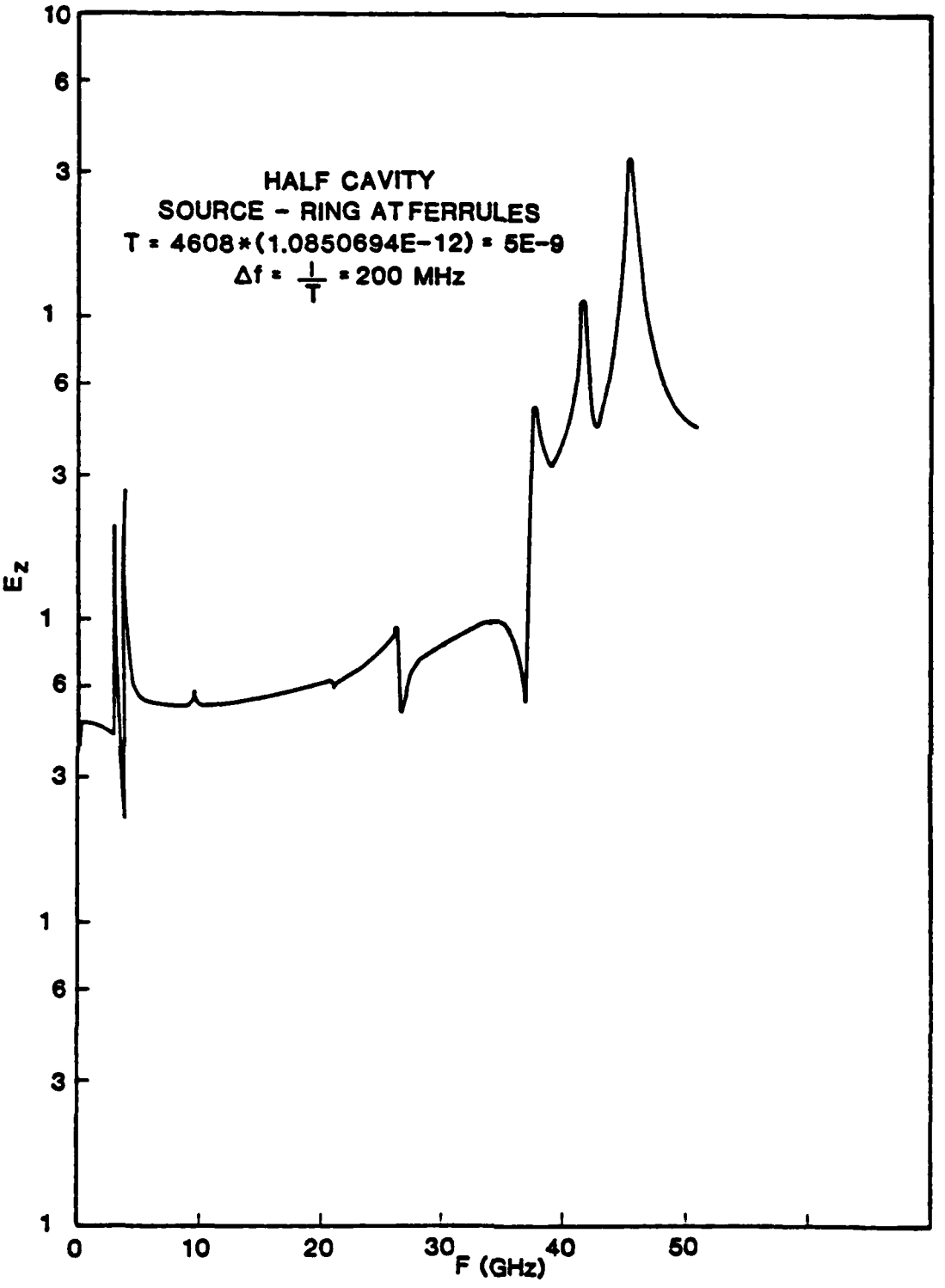

FIGURE 5.4 By doubling the sampling rate (to every 200 MHz) the resonance and source are resolved, but the high frequency amplitudes have grown.

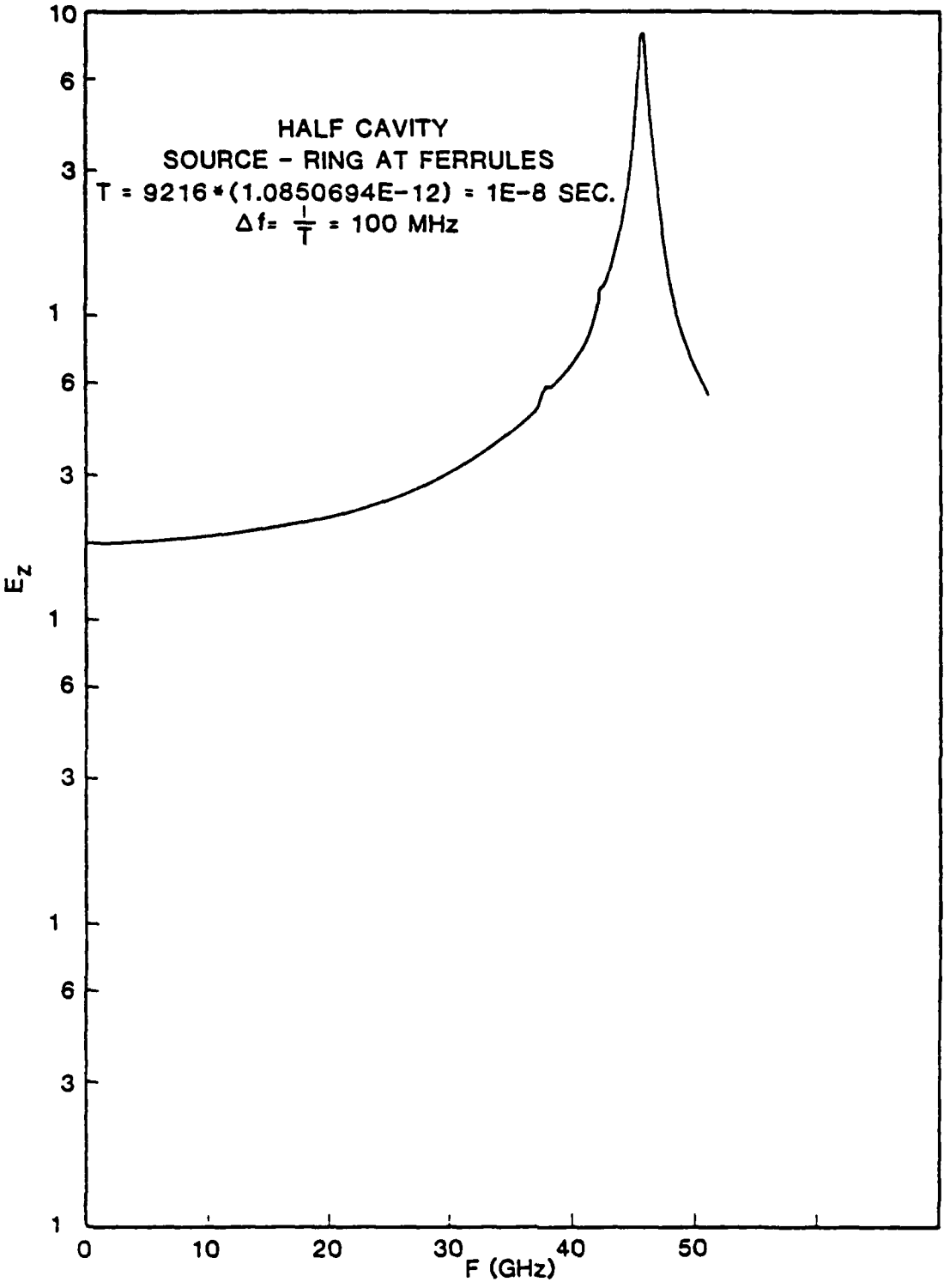

FIGURE 5.5 - After doubling the sampling rate again (to every 100 MHz) the enormous amplitude at high frequency has obscured the area of interest.

CHAPTER VI
CONCLUSIONS AND RECOMMENDATIONS

It has been pointed out to the author, that the shape of the predicted ω-β is quite unlike the curves which are characteristic of staggered slot coupled cavity circuits (first derivative zero at $\beta p=0$ and π, and the second derivative changing signs at approximately $\beta p=\pi/2$). While this objection is true, it is a fact that may be used to one's advantage. By applying a least-squares fit to a cubic function with zero first derivatives at the end points (see Appendix D), it is possible to determine a curve which is fairly close to the measured one. Figure 6.1 demonstrates this method, where the center points of the error bars has been used for the data in equation C.2. The predicted curves look very much as expected now. The maximum error, which occurs at the upper cutoff of the 160^0 slot, is now about 3.9%.

While this project has suffered from some problems, especially in getting a desirable level of resolution, we have obtained our primary objective. That is, we have shown that an existing plasma simulation code may be used to predict, to a fair degree of accuracy, the cold circuit characteristics of a microwave circuit.

A very promising result is that the accuracy was not cost-limited, but rather was limited by the stability problem as explained in Chapter V. This is promising because if we were cost-limited, we would be at the

mercy of the computer industry. That is, no further significant progress could be made until a faster, more efficient computer was built. As is, there is good hope of solving the problem and going on to improved solutions.

We give now some cost figures to illustrate the typical expense of this method. The two runs (three and four cavities) needed to find the data for the 160^0 slot shown in Figure 6.1 were performed at a combined cost of under $150. These runs were performed overnight in batch mode on a slow que (low priority), which results in a charge of $12 per CPU hour. Therefore, the two runs required about 12 CPU hours on the VAX 11/780. This machine has a speed of approximately 0.5 Mflop.

Future investigation should yield solutions to the high frequency instability. The solution may be a combination of changing source methods, grid location, and applying low-pass filters to the fields in the numerical algorithms.

Subsequent to the completion of this project, the high frequency noise problem experienced by the author was verified in a run performed by MRC personnel. It should be noted that this problem is unique to the cylindrical coordinate version of the code. The rectangular version has been in existence for some time, and due to numerous test cases, there is a high level of confidence in its accuracy. Further work is currently being done at MRC to determine the source of this problem and to alleviate it.

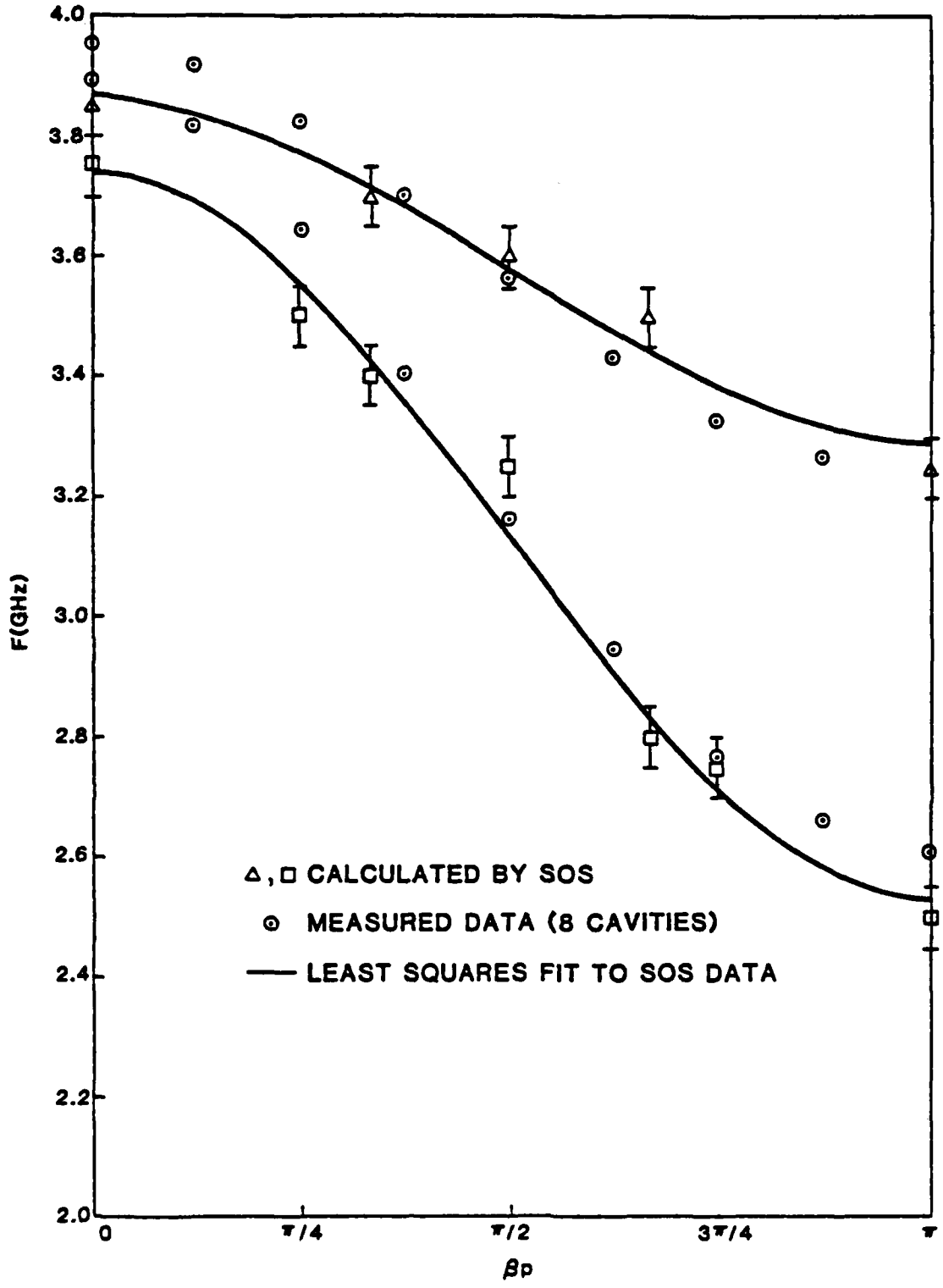

FIGURE 6.1 - Measured and calculated values for the Brillouin plot of the coupled cavity circuits. By applying a least squares fit to the calculated data, we see that it agrees quite well with the measured data. In fact, over the middle one third of the band, which is the area of interest, the agreement is everywhere within 1% error.

APPENDIX A

A DERIVATION OF THE SECOND-ORDER ACCURACY OF THE CENTERED-DIFFERENCE DERIVATIVE FOR A NON-UNIFORM GRID

This appendix shows that, under certain conditions, the centered difference approximation to the derivative of a function will be accurate to second order without the restriction of a uniform grid. The significance of this fact is that it demonstrates both the flexibility and the integrity of the field algorithms used in this study.

The centered difference formula is given by

$$F'(x_i) = \frac{f(x_{i+1})-f(x_{i-1})}{x_{i+1}-x_{i-1}}$$

where f denotes the true function (whose values are known) and F' denotes the approximation to the true derivative f' (whose value is not known). Now, if all derivatives of f exist on the interval $x_{i-1} \leq x \leq x_{i+1}$, then f may be expanded in a Taylor series by defining

$$h_i \equiv x_i - x_{i-1}$$

so that

$$x_{i-1} = x_i - h_i$$

$$x_{i+1} = x_i + h_{i+1}.$$

Then the expansion is

$$f(x_i-h_i) = f(x_i)-h_i f'(xi)+ \frac{h_i^2}{2} f''(xi)\frac{h_i^3}{3!} f'''(x_i)+\ldots$$

$$f(x_i+h_{i+1}) = f(x_i)+h_{i+1}f'(x_i) + \frac{h_{i+1}^2}{2} f''(x_i) + \frac{h_{i+1}^3}{3!} f'''(x_i)+\ldots$$

and the numerical derivative is

$$F'(x_i) = \frac{1}{h_{i+1}+h_i}\{(h_{i+1}+h_i)f'(x_i)+\tfrac{1}{2}(h_{i+1}^2-h_i^2)f''(x_i)$$

$$+\frac{1}{3!}(h_{i+1}^3+h_i^3)f'''(x_i)+\ldots\}$$

$$= f'(x_i)+\tfrac{1}{2}(h_{i+1}-h_i)f''(x_i)+\frac{(h_{i+1}^3+h_i^3)}{6(h_{i+1}+h_i)}f'''(x_i)+\ldots \qquad (A.1)$$

From which it is obvious that second order accuracy $[O(h^2)]$ is obtained for the uniform spacing case; i.e. $h_{i+1}= h_i$. However, if we require the x_i to be a function of a uniformly spaced parameter η,

$$\eta_i = \eta_o+(i-1)\delta\eta \qquad \delta\eta = \text{constant} \qquad (A.2)$$

then second order accuracy may be retained without the stringent requirement of a uniform grid.

Proof:

The functional dependence may be expressed as

$$x_i-x_o = a(\eta_i-\eta_o)+b(\eta_i-\eta_o)^2 \qquad (A.3)$$

and (A.1) may be rewritten as

$$F'(x_i) = f'(x_i)+\tfrac{1}{2}(x_{i+1}-2x_i+x_{i-1})f''(x_i)+\ldots$$

$$= f'(x_i)+\tfrac{1}{2}\{[x_o+a(\eta_{i+1}-\eta_o)+b(\eta_{i+1}-\eta_o)^2]$$

$$-2[x_o+a(\eta_i-\eta_o)+b(\eta_i-\eta_o)^2]+[x_o+a(\eta_{i-1}-\eta_o)+b(\eta_{i-1}-\eta_o)^2]\}f''(x_i)+\ldots$$

Now we make use of (A.2)

$$\eta_{i+1}-\eta_o = i\delta\eta; \qquad \eta_i-\eta_o = (i-1)\delta\eta; \qquad \eta_{i-1}-\eta_o = (i-2)\delta\eta$$

So that the numerical derivative reduces to

$$\begin{aligned} F'(x_i) &= f'(x_i)+\tfrac{1}{2}\{\left[a(i\delta\eta)+b(i\delta\eta)^2\right]-2\left[a(i-1)\delta\eta+b(i-1)^2(\delta\eta)^2\right] \\ &\quad +\left[a(i-2)\delta\eta+b(i-2)^2(\delta\eta)^2\right]\}f''(x_i)+\ldots \\ &= f'(x_i)+\tfrac{1}{2}\{a\delta\eta\left[i-2(i-1)+(i-1)+(i-2)\right]+b\delta\eta^2\left[i^2-2(i-1)^2+(i-2)^2\right]\} \\ &= f'(x_i)+b\delta\eta^2 f''(x_i)+\ldots \end{aligned}$$

Thus, $F'(x_i) = f'(x_i)+O(\delta\eta^2)$

and the numerical derivative is accurate to second order.

APPENDIX B
THE DISCRETE FOURIER TRANSFORM

This appendix formulates the DFT pair which is used in this report to gain frequency information from a limited time history of the fields. Although these equations may be found in texts on signal processing [5], it seemed well to reproduce them here to clarify the relation between the generalized parameters and the parameters of interest to us, which are time and frequency. This also shows the tradeoff between computer cost (total number of samples) and resolution (spacing in frequency samples).

In general, a function, f(t), on the interval $0 \leq t \leq T$ can be expressed as an infinite sum of exponentials

$$f(t) = \sum_{n=-\infty}^{\infty} C_n \, e^{j(2n\pi/T)t}$$

If the function is sampled at discrete points such that

$$t = \frac{mT}{N} \qquad m = 1, 2, 3, \ldots, N$$

then

$$f(t) = f(m) = \sum_{n=-\infty}^{\infty} C_n e^{j(2n\pi/N)m}.$$

Now, we can take advantage of the periodicity of the exponential by substituting $K+\ell N$ for n, where K takes on values only in the range from 1 to N. Then we have

$$f(m) = \sum_{\ell=-\infty}^{\infty} \sum_{K=1}^{N} C_{K,\ell} \, e^{j(2K\pi/N)m} \, e^{j(2\ell N\pi/N)m}$$

$$= \sum_{\ell=-\infty}^{\infty} \sum_{K=1}^{N} C_{K,\ell} \, e^{j(2K\pi/N)m}$$

$$= \sum_{K=1}^{N} e^{j(2K\pi/N)m} \sum_{\ell=-\infty}^{\infty} C_{K,\ell}$$

The last term is merely a summation of constants, so we can define a new constant

$$F(K) \equiv \sum_{\ell=-\infty}^{\infty} C_{K,\ell} \ .$$

Thus

$$f(m) = \sum_{K=1}^{N} F(K)\, e^{j(2K\pi/N)m}$$

or equivalently

$$f(m) = \sum_{n=0}^{N-1} F(n) e^{j(2n\pi/N)m} \ .$$

In order to evaluate the coefficients F(n), we multiply both sides by $e^{-j2\pi\ell m/N}$ and sum from m=0 to N-1.

$$\sum_{m=0}^{N-1} f(m)e^{-j2\pi\ell m/N} = \sum_{m=0}^{N-1}\sum_{n=0}^{N-1} F(n)e^{j2\pi m(n-\ell)/N} \ . \qquad (B.1)$$

At this point, we make use of the orthogonality relation

$$\sum_{m=0}^{N-1} e^{j2\pi mr/N} = \begin{cases} 1 & r=kN \qquad k \text{ an integer} \\ 0 & \text{otherwise} \end{cases}$$

By letting $n-\ell=r$ in (B.1), we see that the RHS is only non-zero if $n=\ell+r=\ell+kN$. Since n=0, 1, ..., N-1 this is only true at one point. For convenience, let ℓ be in the range 0 to N-1, then k must be zero for the condition to be satisfied. Thus,

$$\sum_{n=0}^{N-1} F(n) \sum_{m=0}^{N-1} e^{j2\, m(n-\ell)/N} = F(\ell)\cdot N$$

and (B.1) becomes (dropping the normalization constant N)

$$\sum_{m=0}^{N-1} f(m)e^{-j2\pi \ell m/N} = F(\ell)$$

and our transform pair is thus

$$\left.\begin{aligned} f(m) &= \sum_{n=0}^{N-1} F(n)e^{j(2n\pi/N)m} \qquad m=0,\ 1,\ 2,\ \ldots,\ N-1 \\ F(n) &= \sum_{m=0}^{N-1} f(m)e^{-j(2m\pi/N)n} \qquad n=0,\ 1,\ 2,\ \ldots,\ N-1 \end{aligned}\right\} \quad (B.2)$$

We define the argument of the exponential as ωt, so that

$$\omega t = 2\pi(mn/N)$$

or equivalently

$$ft = mn/N.$$

We have already seen that the time is given by

$$t = \frac{mT}{N}$$

and

$$T \equiv Nt_o$$

So that

$$t = mt_o$$

and

$$f = \frac{n}{Nt_o}.$$

APPENDIX C

A LEAST SQUARES FIT TO A CUBIC POLYNOMIAL

The general equations for a least squares fit of a discrete set of data points to a polynomial of any order may be found in most texts on numerical analysis [9]. However, with the inclusion of boundary conditions on the curve, some of the variables may be eliminated and the equations are changed. For our problem, the value of the curve at the endpoints is not known, but the first derivative is. This appendix, therefore, develops the equations necessary to find the cubic curve which minimizes the square of the error from the data points while retaining a zero first derivative at the endpoints.

Given a set of data points $[x_i;y_i]$ $i=1, 2, \ldots, m$ on the interval $0 \leq x \leq 1$ (note that all intervals may be normalized to this) and the cubic *interpolant*

$$Y=a+bx+cx^2+dx^3$$

and the constraints $\frac{dY}{dx} = 0$ at the endpoints. We wish to minimize the error

$$E = \sum_{i=1}^{m} (Y_i-y_i)^2$$

with respect to the variables a, b, c, and d. However, we can eliminate two of the variables because of the constraints.

$$Y' = \frac{dY}{dx} = b+2c+3dx^2$$

$$Y'(0) = b = 0$$

and

$$Y'(1) = 2c+3d = 0$$

$$c = -\frac{3}{2} d$$

So that

$$Y = a+dx^2 \left(x-\frac{3}{2}\right)$$

Now we minimize the error with respect to the two variables, a and d.

$$\frac{\partial E}{\partial a} = 2 \sum_{i=1}^{m} (Y_i - y_i) \frac{\partial Y_i}{\partial a} = 0$$

$$\frac{\partial E}{\partial d} = 2 \sum_{i=1}^{m} (Y_i - y_i) \frac{\partial Y_i}{\partial d} = 0$$

but we see from (C.1) that

$$\frac{\partial Y_i}{\partial a} = 1$$

$$\frac{\partial Y_i}{\partial d} = x_i^2 (x_i - 3/2)$$

therefore our equations are

$$\left.\begin{aligned} &\sum_{i=1}^{m} (Y_i - y_i) = 0 \\ &\sum_{i=1}^{m} (Y_i - y_i) x_i^2 (x_i - 3/2) = 0 \end{aligned}\right\} \quad (C.2)$$

where

$$Y_i = a + d x_i^2 (x_i - 3/2).$$

So we have two equations from which our two unknowns (a and d) may be found.

REFERENCES

[1] M.A. Allen and G.S. Kino, "On the Theory of Strongly Coupled Cavity Chains," IRE trans. on Microwave Theory and Techniques, pp. 362-372, May 1960.

[2] H.J. Curnow, "A General Equivalent Circuit for Coupled-Cavity Slow-Wave Structures," IEEE trans. on Microwave Theory and Techniques, pp. 671-675, September 1965.

[3] B. Goplen, R.J. Barker, R.E. Clark, J. McDonald, User's Manual for SOS/Version-September 1983, Mission Research Corp. Report, MRC/WDC-R-065.

[4] K. Halbach, et. al., "Properties of the Cylindrical RF Cavity Evaluation Code SUPERFISH," Proc. of the 1976 Proton Linear Accelerator Conf., Chalk River Nuclear Laboratories, Chalk River, Ontario, September 14-17, 1976. pp. 122-128.

[5] A.V. Oppenheim and R.W. Schafer, Digital Signal Processing, Prentice-Hall, Englewood Cliffs, NJ, p. 89.

[6] B. Goplen, et. al., Op. Cit., pp. 3-18.

[7] R.F. Harrington, Time-Harmonic Electromagnetic Fields, McGraw-Hill, New York, p. 214.

[8] T. Moreno, Microwave Transmission Design Data, McGraw-Hill, New York, 1948.

[9] R.L. Burden, J.D. Faires, and A.C. Reynolds, Numerical Analysis, second edition, Prindle, Weber, & Schmidt, Boston, MA, 1981, p. 324.

MISSION
of
Rome Air Development Center

RADC plans and executes research, development, test and selected acquisition programs in support of Command, Control Communications and Intelligence (C^3I) activities. Technical and engineering support within areas of technical competence is provided to ESD Program Offices (POs) and other ESD elements. The principal technical mission areas are communications, electromagnetic guidance and control, surveillance of ground and aerospace objects, intelligence data collection and handling, information system technology, ionospheric propagation, solid state sciences, microwave physics and electronic reliability, maintainability and compatibility.

END

FILMED

3-86

DTIC